



# Shape Models of Lucy Targets (3548) Eurybates and (21900) Orus from Disk-integrated Photometry

Stefano Mottola<sup>1</sup> , Stephan Hellmich<sup>1,5</sup> , Marc W. Buie<sup>2</sup> , Amanda M. Zangari<sup>2,6</sup> , Robert D. Stephens<sup>3</sup> , Mario Di Martino<sup>4</sup> , Gerrit Proffe<sup>1</sup> , Simone Marchi<sup>2</sup> , Catherine B. Olkin<sup>2,7</sup> , and Harold F. Levison<sup>2</sup>

<sup>1</sup>Institute of Planetary Research, DLR, Rutherfordstr. 2, D-12489 Berlin, Germany; [stefano.mottola@dlr.de](mailto:stefano.mottola@dlr.de)

<sup>2</sup>Southwest Research Institute, 1050 Walnut Street, Boulder, CO 80302, USA

<sup>3</sup>Center for Solar System Studies, 11355 Mount Johnson Ct., Rancho Cucamonga, CA 91737, USA

<sup>4</sup>INAF—Osservatorio Astrofisico di Torino, Via Osservatorio 20, I-10025 Pino Torinese, TO, Italy

Received 2022 May 18; revised 2022 December 15; accepted 2022 December 16; published 2023 January 30

## Abstract

We use our new light curves, along with historical data, to determine the rotation state, photometric properties, and convex shape models of the targets of the Lucy mission (3548) Eurybates and (21900) Orus. We determine a retrograde spin for both targets, with sidereal rotation periods of  $8.7027283 \pm 0.0000029$  h and  $13.486190 \pm 0.000017$  h, respectively. The phase curves of both objects are nearly linear in the phase-angle range observable from Earth and lack a pronounced opposition effect. Unsupervised classification of these phase curves by the Penttilä et al. tool suggests that Eurybates and Orus belong to the C and D taxonomic types, respectively, thereby independently confirming past classifications based on their spectral slope. Time-resolved color-index measurements show no systematic color variations correlated with rotation for either target at the 1% level, suggesting that no variegation is present on a hemispherical scale for any of the objects. Comparison of the shape models with stellar occultation data available for the two objects from the program by Buie et al. allows us to resolve the longitude ambiguity of the orientations of the spin axes and derive unique pole solutions for both targets. Furthermore, scaling the shape models to match the occultation chords produces accurate sizes and geometric albedos for both objects. The derived surface-equivalent spherical diameters are  $D_s = 69.3 \pm 1.4$  km and  $D_s = 60.5 \pm 0.9$  km for Eurybates and Orus, respectively, while the geometric albedo in the  $H$ ,  $G_1$ ,  $G_2$  system is  $p_V(H, G_1, G_2) = 0.044 \pm 0.003$  and  $p_V(H, G_1, G_2) = 0.040 \pm 0.002$  for Eurybates and Orus, respectively.

*Unified Astronomy Thesaurus concepts:* Jupiter trojans (874); Light curves (918); CCD photometry (208)

*Supporting material:* machine-readable tables

## 1. Introduction

Lucy is a NASA mission of the Discovery class that will perform a fly-by tour through both L4 and L5 Jupiter Trojan clouds (Levison et al. 2021; Olkin et al. 2021). This paper is the fourth of a series (Buie et al. 2018, 2021; Mottola et al. 2020) devoted to characterizing the rotational state and the photometric properties and to deriving sizes and shape models of the Lucy targets from disk-integrated photometry and stellar occultation observations.

Among the Lucy targets are (3548) Eurybates and (21900) Orus, both located in the L4 swarm, for which close encounters are planned in 2027 August and 2028 November, respectively.

Eurybates has a moderate orbital inclination of  $8^\circ$ . Tedesco et al. (2004) report an IRAS-derived geometric albedo  $p_V = 0.054 \pm 0.007$  and a mean diameter  $D_s = 72.1 \pm 4.1$  km. Based on NEOWISE radiometry, Grav et al. (2012) report a

geometric albedo  $p_V = 0.052 \pm 0.007$  and a spherical-equivalent diameter  $D_s = 63.885 \pm 0.299$  km, while Usui et al. (2011) determined a mean geometric albedo  $p_V = 0.060 \pm 0.007$  and a mean diameter  $D_s = 68.40 \pm 3.92$  km from AKARI mid-infrared data. With its size, Eurybates is the largest surviving member of the only firmly established collisional families in the Trojan region (Roig et al. 2008; Brož & Rozehnal 2011; Milani et al. 2017). Fornasier et al. (2007)—based on visible-range spectroscopy—classified Eurybates and the majority of the observed members of its family as belonging to the taxonomic type C. This classification makes Eurybates and its family quite unique, since only about 10% of the Jupiter Trojans classified so far belong to this group (Roig et al. 2008).

Stephens (2010) and Mottola et al. (2011) reported the first independent determinations of the synodic rotation period for Eurybates with  $8.72 \pm 0.01$  h and  $8.711 \pm 0.009$  h, respectively. Mottola et al. (2016) used a partial data set from the work reported in this paper to perform the first light-curve inversion for Eurybates, determine its sidereal period ( $P_{\text{sid}} = 8.702724 \pm 0.000009$  h), establish its retrograde rotation, and derive a preliminary convex shape model. Souza-Feliciano et al. (2020) performed visible spectroscopy of Eurybates at three discrete rotational phases and suggested the presence of spectral slope variations with rotation, implying compositional heterogeneity over the surface.

Noll et al. (2020) discovered the existence of a  $\sim 1$  km sized satellite—Queta—in orbit around Eurybates from images obtained with the Hubble Space Telescope. The presence of a

<sup>5</sup> Currently at the Laboratory of Astrophysics, École Polytechnique Fédérale de Lausanne (EPFL), Switzerland.

<sup>6</sup> Amanda Zangari is currently an MIT Lincoln Laboratory employee. No Laboratory funding or resources were used to produce the results/findings reported in this publication.

<sup>7</sup> Currently at Muon Space, 2250 Charleston Road, Mountain View, CA 94043, USA.



satellite, a likely remnant of the collisional past of the object, holds the promise of an accurate determination of the bulk density of the system, once its orbit is firmly established.

Orus, too, lies on an orbit with an inclination of  $8^\circ$ . Usui et al. (2011) estimated a geometric albedo  $p_V = 0.083 \pm 0.015$  and a mean diameter  $D_s = 53.87 \pm 4.08$  km from AKARI data, while Grav et al. (2012) determined a geometric albedo  $p_V = 0.075 \pm 0.014$  and a mean diameter  $D = 50.810 \pm 0.809$  km from NEOWISE radiometry. Emery et al. (2010) measured low-resolution near-IR (NIR) spectra for Orus that place the object in the region of the so-called *redder objects* in their color-color diagram. Such a region is associated with the taxonomic D type (Emery et al. 2010; Levison et al. 2017). No membership to a collisional family has yet been proposed, and no satellite has been discovered orbiting around Orus, so far.

Mottola et al. (2011) reported the first determination of the rotation period of Orus, while Mottola et al. (2016), based on a subset of the data reported in this paper, obtained preliminary results about Orus's sidereal rotation period ( $P_{\text{sid}} = 13.48617 \pm 0.00007$  h), its retrograde rotation, and a preliminary convex shape model.

## 2. Observations and Data Reduction

This paper reports unpublished photometric observations of (3548) Eurybates and (21900) Orus acquired during most apparitions of the L4 Trojan cloud in the decade between the end of year 2011 and the end of 2021, thereby covering nearly one complete orbital cycle around the Sun. The observations were performed with the 1.2 m telescope at Calar Alto, Spain; the two 24" telescopes at the Sierra Remote Observatories (SRO), Auberry, CA, USA, owned and operated by the Southwest Research Institute (SwRI); 1.0 m telescopes from the Las Cumbres Observatory Global Telescope (LCOGT) network; and the 1.2 m MONET South telescope, Sutherland, South Africa. All of the observations were either performed robotically or operated remotely from the observer's home institution.

The bulk of the observations were performed in the Cousins  $R_C$  filter, in the Sloan Digital Sky Survey (SDSS)  $r'$  filter, or in a  $VR$  bandpass, according to the respective telescope's instrumentation, in order to maximize throughput. However, whenever possible, we also acquired frames in the Johnson  $V$  band, in order to allow an accurate determination of the  $H$ -value. The 2020 campaign in Calar Alto was designed to detect possible rotation-induced color variations. For this reason we acquired high-cadence time series with  $B$ ,  $V$ ,  $R$ , and  $I$  Johnson-Cousins filters. The observations were conducted on consecutive nights for the period necessary to cover at least two complete rotations of the targets, thereby allowing for confirmation in the case of a positive color variation detection. Details about the observatories, observers, and observing geometry are given in Tables 1 and 2 for Eurybates and Orus, respectively. The observing techniques, the instrumentation, the data reduction methods, and the software tools used for these observations closely follow those described extensively in Mottola et al. (2020) for the respective telescopes.

In addition to the new data reported here, for the shape inversion and photometric analysis we used dense historical data from Mottola et al. (2011), Stephens (2010), Pál et al. (2020), and Stephens & Warner (2021). Furthermore, we made use of sparse data from the Gaia Second Data Release (Gaia Collaboration et al. 2018), the ZTF project (Bellm et al. 2019;

IRSA 2022), the Pan-STARRS1 DR2 database (Flewelling et al. 2020), and the ATLAS project (Tonry et al. 2018), retrieved with the methods described in Mottola et al. (2020).

## 3. Convex Shape Modeling

The photometric observations described in the previous section have been used to apply the convex inversion technique described in Kaasalainen et al. (2001, 2002) and references therein to retrieve the rotation state, the photometric properties, and a convex approximation of the shape of the targets. Although methods have been proposed for the nonconvex inversion of light curves (Kaasalainen & Torppa 2001; Viikinkoski et al. 2015; Bartczak & Dudziński 2018), those produce models that are intrinsically nonunique when applied to light-curve data alone and can result in a variety of shapes that can equally fit the observed data within the photometric uncertainties (Viikinkoski et al. 2017). This ambiguity is particularly severe for disk-integrated photometric observations of Trojan asteroids performed from Earth, since they are always performed at small solar phase angles and contain virtually no information about concavities (Durech & Kaasalainen 2003). The models from the convex inversion technique, on the other hand, are unique (Kaasalainen & Torppa 2001) and result in a polyhedral approximation of the body shape if the body is globally convex, or approach the convex hull of the body if the object contains global concavities.

For the purpose of convex inversion, we used the implementation and notation described in Mottola et al. (2020), with further modifications and extensions as described in the following subsections.

Formal  $1\sigma$  uncertainties on the rotational and photometric parameters have been estimated by using the statistical *bootstrap method* (Press et al. 1992). To this end, 500 synthetic data sets have been generated by randomly sampling the original data set, on a light-curve-by-light-curve basis, and by running corresponding instances of the inversion procedure. The uncertainties were then determined by computing the standard deviation of each resulting best-fit model parameter.

### 3.1. Levenberg–Marquardt Nonlinear Optimization

The core optimization in the convex inversion method is performed via Levenberg–Marquardt (LM) nonlinear fitting (Kaasalainen & Torppa 2001). In order to improve the robustness and performance of the LM method for problems with a large number of residuals, we have applied several modifications to the original method as suggested by Transtrum et al. (2011). In particular, we have implemented the methods of *bold acceptance*, *delayed gratification*, and *modified damping matrix* that help mitigate the problems of *slow convergence* and *parameter evaporation* (Transtrum & Sethna 2012).

### 3.2. Relative, Absolute, and Semi-absolute Photometry

The convex inversion technique exploits the observed variations in the brightness of an unresolved body in order to retrieve information about its spin state, shape, and photometric properties. These variations have both rotational and long-term components. The rotational component mostly carries information about the body elongation (or about its  $a$  and  $b$  semiaxes in the body-fixed  $X$ - $Y$  plane). The long-term component, on the other hand, can carry information about the vertical extent of

**Table 1**  
Observational Circumstances for (3548) Eurybates

Date (UT)	$\lambda$ (deg J2000)	$\beta$	$\alpha$ (deg)	$r$ (au)	$\Delta$ (au)	$\lambda$ (PAB) $\beta$ (deg J2000)		Band	Observatory	Observers
2012 Feb 25.9	126.5	+9.8	6.056	4.9210	4.0506	129.4	+9.0	$R_C$	493	SMo, SH
2012 Feb 28.9	126.2	+9.8	6.580	4.9228	4.0760	129.4	+8.9	$R_C$	493	SMo, SH
2012 Mar 28.9	124.7	+9.0	10.466	4.9406	4.4210	130.0	+8.6	$R_C$	493	SMo, SH
2012 Apr 25.9	126.0	+8.2	11.710	4.9583	4.8521	132.0	+8.2	$R_C$	493	SMo, SH
2013 Feb 4.1	169.1	+8.4	6.265	5.1498	4.3091	166.0	+7.7	$R_C$	493	SMo, SH
2013 Apr 2.0	162.1	+8.1	5.710	5.1890	4.3073	164.9	+7.4	$R_C$	493	SMo, SH
2013 May 2.9	160.4	+7.2	9.861	5.2100	4.6641	165.3	+6.9	$R_C$	493	SMo, SH
2013 May 7.9	160.4	+7.1	10.272	5.2135	4.7371	165.5	+6.8	$R_C$	493	SMo, SH
2014 Feb 2.2	202.0	+4.6	9.834	5.3872	4.9549	197.1	+4.4	$R_C$	493	SMo, SH
2014 Feb 8.1	202.0	+4.6	9.389	5.3906	4.8716	197.3	+4.4	$R_C$	493	SMo, SH
2014 Apr 22.9	195.0	+4.2	3.287	5.4328	4.4679	196.6	+3.9	$R_C$	493	SMo, SH
2014 Apr 23.9	194.9	+4.2	3.467	5.4333	4.4729	196.6	+3.8	$R_C$	493	SMo, SH
2017 Aug 1.5	277.7	-8.3	5.614	5.5692	4.6862	280.5	-7.6	$r'$	Q63	MB, AZ
2017 Aug 2.2	277.7	-8.3	5.707	5.5690	4.6910	280.5	-7.6	$r'$	W85	MB, AZ
2018 Aug 2.8	310.8	-9.9	1.858	5.3951	4.3926	310.7	-9.0	$r'$	K95	SMo, SH
2018 Aug 10.7	309.8	-9.9	2.370	5.3905	4.3970	310.5	-9.0	$r'$	K95	SMo, SH
2018 Aug 15.9	309.1	-9.9	3.114	5.3874	4.4099	310.4	-9.0	$r'$	K95	SMo, SH
2018 Sep 30.2	305.7	-9.0	9.437	5.3605	4.8077	310.5	-8.6	VR	G80	MB
2018 Oct 2.1	305.7	-8.9	9.604	5.3593	4.8341	310.6	-8.5	VR	G80	MB
2018 Oct 14.1	305.9	-8.6	10.360	5.3521	5.0024	311.1	-8.4	VR	G80	MB
2018 Oct 28.1	306.6	-8.2	10.709	5.3435	5.2117	312.0	-8.2	VR	G80	MB
2018 Nov 6.1	307.4	-8.0	10.646	5.3379	5.3478	312.8	-8.1	VR	G80	MB
2019 Jun 29.1	348.1	-8.0	10.713	5.1849	4.7711	342.7	-7.7	$R_C$	493	SH, SMo
2019 Jul 9.1	348.2	-8.2	9.997	5.1782	4.6246	343.2	-7.8	$R_C$	493	SH, SMo
2019 Jul 30.1	347.4	-8.6	7.520	5.1641	4.3619	343.6	-7.9	$V, R_C$	493	SH, SMo
2019 Aug 9.9	346.4	-8.7	5.768	5.1567	4.2592	343.6	-7.9	$V, R_C$	493	SH, SMo
2019 Aug 30.0	344.1	-8.8	2.305	5.1432	4.1505	343.3	-7.9	$R_C$	493	SH, SMo
2019 Jun 30.4	348.1	-8.1	10.636	5.1840	4.7512	342.8	-7.7	VR	G80	MB
2019 Jul 28.4	347.5	-8.5	7.757	5.1652	4.3795	343.6	-7.9	VR	G80	MB
2019 Aug 29.4	344.2	-8.8	2.405	5.1437	4.1524	343.3	-7.9	VR	G80	MB
2019 Sep 30.3	340.2	-8.4	5.194	5.1222	4.2132	342.7	-7.6	VR	G80	MB
2019 Oct 20.2	338.6	-7.9	8.349	5.1088	4.3901	342.7	-7.3	VR	G80	MB
2020 Aug 22.0	24.0	-4.6	9.709	4.9151	4.2649	19.1	-4.3	$V, R_C$	493	SMo, SH
2020 Aug 25.1	23.9	-4.6	9.333	4.9134	4.2264	19.2	-4.3	$V, R_C$	493	SMo, SH
2020 Oct 11.9	18.8	-4.2	0.952	4.8859	3.8911	19.0	-3.8	$B, R_C, I$	493	SMo, SH
2020 Oct 12.9	18.9	-4.2	0.881	4.8865	3.8909	19.0	-3.8	$B, R_C, I$	493	SMo, SH
2020 Oct 13.9	18.8	-4.2	0.952	4.8859	3.8911	19.0	-3.8	$B, V, R_C, I$	493	SMo, SH
2020 Oct 14.9	18.6	-4.2	1.071	4.8854	3.8915	18.9	-3.8	$B, V, R_C, I$	493	SMo, SH
2021 Aug 18.1	60.9	+0.7	12.212	4.7613	4.7554	54.7	+0.7	$R_C$	493	SMo
2021 Aug 20.1	61.1	+0.8	12.240	4.7608	4.7242	55.0	+0.8	$R_C$	493	SMo
2021 Dec 27.9	53.5	+3.0	8.087	4.7373	3.967	57.6	+2.8	$R_C$	493	SMo
2021 Dec 30.9	53.3	+3.0	8.567	4.7370	3.9992	57.6	+2.8	$R_C$	493	SMo

**Note.** This table is an excerpt. The observational circumstances for all of the observation nights are reported in the online material.  $\lambda$  and  $\beta$  are the topocentric ecliptic longitude and latitude of the target, respectively.  $\alpha$  is the solar phase angle,  $r$  is the heliocentric distance, and  $\Delta$  is the topocentric range of the target.  $\lambda$  and  $\beta$  (PAB) are the topocentric ecliptic longitude and latitude of the phase-angle bisector, as defined in Harris et al. (1984). The last column reports the initials of the observers. (This table is available in its entirety in machine-readable form.)

the body (or the  $c/a$  ratio). For rotation periods that are not much longer than a typical observing session, relative photometric measurements are generally adequate for capturing the rotational component on subsequent nights. Recording the long-term component, on the other hand, requires accurate absolutely calibrated measurements that are consistent over many apparitions, which is a much more demanding task for a ground-based observer. Therefore, photometric errors in

ground-based light curves of asteroids are often dominated by the uncertainties of the absolute-calibration zero-points, rather than by their signal-to-noise ratio (S/N). In such cases, if absolute magnitudes are used in the shape inversion, the calibration errors tend to obfuscate the signature of the best solution in the merit function. Although this issue has recently been partially mitigated by the advent of accurate all-sky photometric catalogs and by the increasing availability of

**Table 2**  
Observational Circumstances for (21900) Orus

Date (UT)	$\lambda$ (deg J2000)	$\beta$	$\alpha$ (deg)	$r$ (au)	$\Delta$ (au)	$\lambda$ (PAB) $\beta$ (deg J2000)		Band	Observatory	Observers
2011 Dec 18.1	89.9	−1.9	0.934	4.9430	3.9616	89.5	−1.7	$R_C$	493	SMo, SH
2011 Dec 18.9	89.8	−1.9	0.748	4.9431	3.9608	89.4	−1.8	$R_C$	493	SMo, SH
2011 Dec 20.0	89.6	−2.0	0.555	4.9431	3.9601	89.4	−1.8	$R_C$	493	SMo, SH
2012 Feb 20.9	84.3	−2.6	10.631	4.9468	4.4809	89.6	−2.5	$R_C$	493	SMo, SH
2012 Feb 22.9	84.3	−2.7	10.777	4.9469	4.5089	89.7	−2.5	$R_C$	493	SMo, SH
2012 Dec 11.1	130.3	−6.7	8.880	4.9852	4.3110	125.8	−6.2	$R_C$	493	SMo, SH
2012 Dec 17.1	130.0	−6.9	8.012	4.9863	4.2410	125.9	−6.4	$R_C$	493	SMo, SH
2012 Dec 18.1	129.9	−6.9	7.867	4.9865	4.2307	126.0	−6.4	$R_C$	493	SMo, SH
2013 Feb 7.9	123.6	−7.8	3.377	4.9967	4.0464	125.2	−7.1	$R_C$	493	SMo, SH
2013 Apr 4.8	120.5	−7.3	11.105	5.0085	4.6498	126.1	−7.1	$R_C$	493	SMo, SH
2014 Jan 26.1	164.9	−9.9	7.180	5.0823	4.2902	161.4	−9.1	$R_C$	493	SMo, SH
2014 Feb 8.1	163.7	−10.2	4.978	5.0859	4.1845	161.3	−9.3	$R_C$	493	SMo, SH
2014 Feb 21.0	162.1	−10.3	2.757	5.0894	4.1253	161.1	−9.4	$R_C$	493	SMo, SH
2014 Feb 24.9	161.7	−10.4	2.361	5.0902	4.1187	161.0	−9.4	$R_C$	493	SMo, SH
2014 Mar 17.9	158.7	−10.3	3.998	5.0962	4.1542	160.5	−9.4	$R_C$	493	SMo, SH
2016 May 26.2	224.9	−5.2	3.925	5.2825	4.3237	226.8	−4.7	$r'$	W86	MB, AZ
2016 May 26.3	224.9	−5.2	3.935	5.2825	4.3237	226.8	−4.7	$r'$	W87	MB, AZ
2016 Jun 3.2	224.0	−5.0	5.385	5.2836	4.3753	226.7	−4.6	$r'$	V37	MB, AZ
2016 Jun 6.2	223.7	−5.0	5.900	5.2840	4.3987	226.6	−4.5	$r'$	W87	MB, AZ
2016 Jun 21.0	222.6	−4.6	8.130	5.2860	4.5445	226.7	−4.3	$r'$	W86	MB, AZ
2016 Jun 22.2	222.5	−4.6	8.288	5.2862	4.5585	226.7	−4.3	$r'$	V37	MB, AZ
2016 Jul 5.9	222.1	−4.3	9.777	5.2879	4.7343	227.0	−4.1	$r'$	W86	MB, AZ
2018 Jul 14.9	289.5	+5.5	1.179	5.2805	4.2686	289.8	+5.0	$R_C$	493	SH, SMo
2018 Jul 15.9	289.4	+5.5	1.283	5.2803	4.2694	289.8	+5.0	$R_C$	493	SH, SMo
2018 Jul 16.9	289.3	+5.5	1.406	5.2802	4.2705	289.7	+5.0	$V, R_C$	493	SH, SMo
2018 Aug 31.2	285.1	+5.6	8.750	5.2733	4.5991	289.4	+5.3	VR	G80	MB
2018 Sep 1.2	285.0	+5.6	8.867	5.2731	4.6117	289.5	+5.3	VR	G80	MB
2018 Sep 4.2	284.9	+5.6	9.192	5.2726	4.6501	289.5	+5.3	VR	G80	MB
2018 Sep 14.1	284.8	+5.6	10.065	5.2710	4.7856	289.9	+5.3	VR	G80	MB
2018 Sep 21.2	285.0	+5.5	10.500	5.2698	4.8884	290.2	+5.3	VR	G80	MB
2019 May 4.4	324.7	+6.8	10.912	5.2250	5.3265	319.2	+6.9	VR	G80	MB
2019 Jun 29.4	327.0	+8.5	8.639	5.2118	4.5040	322.7	+7.9	VR	G80	MB
2019 Jul 2.4	326.8	+8.6	8.260	5.2111	4.4691	322.7	+8.0	VR	G80	MB
2019 Jul 6.4	326.6	+8.7	7.725	5.2101	4.4257	322.8	+8.0	VR	G80	MB
2019 Nov 24.1	319.7	+7.9	10.784	5.1743	5.2769	325.2	+8.0	VR	G80	MB
2019 Jun 2.1	327.0	+7.7	10.877	5.2183	4.8820	321.6	+7.4	$V, R_C$	493	SH, SMo
2019 Jul 11.1	326.3	+8.8	7.039	5.2090	4.3784	322.8	+8.1	$V, R_C$	493	SH, SMo
2019 Aug 4.0	323.8	+9.3	3.022	5.2031	4.2189	322.5	+8.4	$V, R_C$	493	SH, SMo
2019 Aug 9.9	323.0	+9.4	2.171	5.2016	4.2034	322.4	+8.5	$V, R_C$	493	SH, SMo
2019 Aug 10.9	322.9	+9.4	2.065	5.2014	4.2018	322.4	+8.5	$V, R_C$	493	SH, SMo
2020 Aug 17.0	0.2	+10.1	6.880	5.1004	4.2563	356.8	+9.3	$B, V, R_C$	493	SH, SMo
2020 Aug 18.0	0.1	+10.1	6.717	5.1002	4.2473	356.8	+9.3	$B, V, R_C$	493	SH, SMo
2020 Aug 19.0	0.0	+10.2	6.554	5.0999	4.2386	356.8	+9.3	$B, V, R_C$	493	SH, SMo
2020 Aug 20.0	359.9	+10.2	6.394	5.0996	4.2304	356.8	+9.3	$B, V, R_C$	493	SH, SMo
2020 Aug 21.0	359.8	+10.2	6.221	5.0993	4.2218	356.8	+9.3	$B, V, R_C$	493	SH, SMo

**Note.** This table is an excerpt. Definition of columns is the same as in Table 1.

(This table is available in its entirety in machine-readable form.)

space-based asteroid photometric data—as in the Gaia (Gaia Collaboration et al. 2018), TESS (Ricker et al. 2014), and K2 (Borucki et al. 2010) surveys—it is often still a problem. Frequent reasons are (1) a small field of view of the imaging system that does not allow for a sufficient number of catalog stars, (2) a nonstandard filter/detector combination that does not allow for robust transformations to a standard photometric system, and (3) use of heterogeneous instrumentation for

different data sets. In such cases it is customary to perform the inversion by using relative magnitudes (normalized to their maximum or average value) in order to obtain a viable solution, thereby sacrificing information about the vertical extent of the body (Bartczak & Dudziński 2019; Kaasalainen & Āurech 2020).

In order to address this issue, which is particularly severe for bodies with a low light-curve amplitude, we have introduced



the concept of what we call—in a rather facetious way—*semi-absolute* photometry. In addition to the two different metrics for absolute and relative photometry (see Mottola et al. 2020 and references therein), we have defined a merit function for the semi-absolute photometry as

$$\chi_{\text{semi-abs}}^2 = \sum_{k,j} \left( \frac{\bar{L}_j^{\text{obs}}}{\sigma_{k,j}} \right)^2 \left( \frac{L_{k,j}^{\text{obs}}}{\bar{L}_j^{\text{obs}}} - \frac{L_{k,j}^{\text{mod}}}{\bar{L}_j^{\text{mod}}} \right)^2 + \lambda \sum_j \left( \frac{\bar{L}_j^{\text{obs}} - \bar{L}_j^{\text{mod}}}{\epsilon_j} \right)^2, \quad (1)$$

where the indices  $j$  and  $k$  run over the light curves and individual data points, respectively, and  $n$  is the total number of light curves. The  $L$  terms represent the intensities, where the superscript specifies whether they are observed or modeled. An overline specifies that the intensity is averaged over the  $j$ th light curve. The term  $\sigma_{k,j}$  represents the photometric uncertainty of the individual data points, expressed in intensity, while  $\epsilon_j$  is the photometric uncertainty of the average observed intensity caused by the error on the zero-point of the  $j$ th light curve. The term  $\lambda$  is a positive coefficient that represents the weight of the contribution of the absolute photometry uncertainty to the merit function, and it can be seen as a Pareto coefficient (see, e.g., Caramia & Dell’Olmo 2008) in a multiobjective optimization. Alternatively,  $\lambda$  can be seen as a regularization coefficient that penalizes solutions that depart from the best-fit phase function. In practice, the residual vector is augmented by the  $n$  elements that contain the residual of the mean intensity for each semi-absolute light curve, with the corresponding elements of the Jacobian matrix being computed as usual for the LM optimization.

With this formalism we effectively separate the contribution of the relative accuracy (first term of the sum; see Mottola et al. 2020) from that of the calibration accuracy (second term), which can therefore be weighted independently through the coefficient  $\lambda$ . As a means to determining an appropriate value for the  $\lambda$  weight, we perform several runs by starting from a value of zero and subsequently increasing it. We then select the value of  $\lambda$  that reduces the absolute photometry residuals, without significantly increasing the relative photometry residual term.

### 3.3. $H$ , $G_1$ , $G_2$ Surface Phase Function

In the convex inversion scheme, the photometric properties of the surface are described through a photometric function. A common and convenient choice is to use a photometric function that is separable in the product of a disk and a surface phase function (see the Appendix). For the disk function we use a linear combination of the Lommel–Seeliger function (to account for the single-scattering component) and the Lambert function (for approximating the multiple-scattering component). As a surface phase function, a simple three-parameter linear exponential expression is often used (Kaasalainen et al. 2001). Although such a linear exponential surface phase function is able to reproduce quite reasonably the phase-angle behavior of many planetary surfaces and has proven to be a successful general-purpose tool for the convex shape inversion (Kaasalainen et al. 2001), it is a simple analytical function that is neither derived from theoretical considerations about light

scattering nor based on empirical analysis of observed photometric data. Two of the most obvious drawbacks of the linear exponential function are (1) the inability to adequately reproduce the opposition surge (Belskaya & Shevchenko 2000) for very small phase angles ( $\leq 2^\circ$ ) and (2) its tendency to assume negative values at very large phase angles. Furthermore, its three model parameters are not readily translated into those of a standard photometric system for phase curves, such as the (now-deprecated) HG system (Bowell et al. 1989) or the IAU-adopted  $H$ ,  $G_1$ ,  $G_2$  (Muinonen et al. 2010) system, widely used by observers. For this reason, in addition to using the linear exponential surface phase function, we also introduce the  $H$ ,  $G_1$ ,  $G_2$  surface phase function for the Lommel–Seeliger–Lambert disk function, which has the property of resulting in sphere-integrated phase curves (Mottola et al. 2020) that directly follow the  $H$ ,  $G_1$ ,  $G_2$  function. With this approach we generalize the definition of the  $H$ ,  $G_1$ ,  $G_2$  surface phase function for Lommel–Seeliger surfaces by Muinonen et al. (2015) by extending it to the Lommel–Seeliger–Lambert disk function, as detailed in the Appendix. One important aspect of the  $H$ ,  $G_1$ ,  $G_2$  model is that it is founded on basis functions that encompass the observed phase functions of a sizable set of asteroids and natural satellites. As such, it has an empirical justification. It is also worth noting that a strong correlation has been found between the location of an object in the  $G_1$ ,  $G_2$  parameter space and its taxonomic type (Penttilä et al. 2016; Shevchenko et al. 2016), which, although no proof, can provide an independent confirmation of a taxonomic classification made through spectral measurements. Further, the use of this function in the convex inversion natively returns model parameters in an IAU-endorsed system. Last but not least, the normalized version of the  $H$ ,  $G_1$ ,  $G_2$  surface phase function only depends on two parameters, as opposed to the three-parameter linear exponential function, thereby making the inversion procedure more stable, even in the case of data sets that do not optimally sample the phase-angle domain.

Our approach is not unsimilar to the one recently described by Martikainen et al. (2021) when determining the phase-curve parameters of a large sample of asteroids from Gaia photometry, although the two methods differ in a number of details. Martikainen et al. (2021), similarly to our approach, derive a surface function based on the  $H$ ,  $G_1$ ,  $G_2$  formalism, although coupled to a Lommel–Seeliger disk function, as opposed to the Lommel–Seeliger–Lambert function used in our case. During the inversion of the photometric properties of the targets, Martikainen et al. (2021) solve for the linear slope  $\beta_S$  of the surface phase function, which is linked to the single parameter  $G_{12}$  (Muinonen et al. 2010). By using this parameter, the authors construct the reference phase curves, by averaging the light-curve brightness over one full rotation for selected phase angles. These reference phase curves are similar, but not identical, to our sphere-integrated phase curves, as the former still contain a weak dependence on the shape of the target (Helfenstein & Veverka 1989). Finally, Martikainen et al. (2021) fit their reference phase curves to derive  $G_1$  and  $G_2$  parameters, as opposed to our approach, where  $G_1$  and  $G_2$  are directly derived in the inversion procedure. In summary, our method represents a more direct approach to the retrieval of the phase-curve parameters and is well suited for the application to well-sampled data sets. The method by Martikainen et al. (2021), on the other hand, due to the simplified parameterization, may offer a more stable solution in the case of sparse and

not optimally sampled data sets. However, all in all these differences should be small enough, so that the two methods should produce results that are directly comparable in most situations.

### 3.4. Direct Facet-area Polyhedral Inversion

The convex inversion method seeks to retrieve a convex approximation of the object’s shape in two steps. First, the extended Gaussian image (EGI; Horn 1984) of the shape is constructed during the inversion process. The EGI of a polyhedron is defined on the unit sphere and associates a scalar field consisting of the surface areas (or the product of the surface area times the facet’s albedo) of the polyhedron facets with the directions defined by the normals to the original facets. The EGI can also be seen as the equivalent in the discrete case of the Gauss surface density for the continuous case. The EGI uniquely defines a convex polyhedron (Minkowski 1897). Furthermore, the light curves produced by a convex object only depend on its EGI, since for a convex object neither shadowing nor self-obstruction is present. However, the EGI lacks explicit information about the shape of the facets and their connectivity. In order to reconstruct the 3D shape of the target from its EGI, the *Minkowski problem* needs to be solved in the second step, for which Lamberg (1993) and Lamberg & Kaasalainen (2001) gave a practical implementation.

Because of the large body of photometric data available for the two observed targets—and their good photometric accuracy—the convex shape was retrieved via direct inversion of the facets’ areas of the EGI as opposed to the inversion of its spherical harmonics expansion (Kaasalainen & Torppa 2001). With this procedure we effectively lift the regularization on the facets’ areas operated by the spherical harmonics functions and can obtain a more realistic approximation of the shape.

Contrary to Kaasalainen & Torppa (2001)—who use a conjugate gradient minimization algorithm for this purpose—we optimize the polyhedron facets’ areas by applying the modified LM method mentioned above. Because the LM method makes explicit use of the quadratic form of the  $\chi^2$  merit function, it arguably offers better convergence and parameter sensitivity than conjugate gradients, at the expense of a higher computational cost. The latter drawback, however, is offset by recent advances in computer technology that make even large problems (of the order of a few thousand residuals) tractable with LM on desktop computers.

The direct facet-area polyhedral inversion was performed by fixing the rotation and photometric models to their best-fit values previously determined via a global smooth-function fit and by leaving only the facets’ areas as free parameters. The number of facets is chosen for each model based on the total number, accuracy, and distribution of the data points and typically ranges from one to a few thousand. We typically performed several shape inversion runs starting from slightly varied initial conditions for the parameter vector and verified that all solutions converged to a nearly identical shape. The reconstruction of the convex shape from its EGI—the Minkowski problem—was performed by using the procedure described in Lamberg (1993) and Lamberg & Kaasalainen (2001).

The orientation of the body reference system and the maximum body dimensions we use in this paper follow the definitions given in Mottola et al. (2020).

## 4. Eurybates

### 4.1. Light Curves

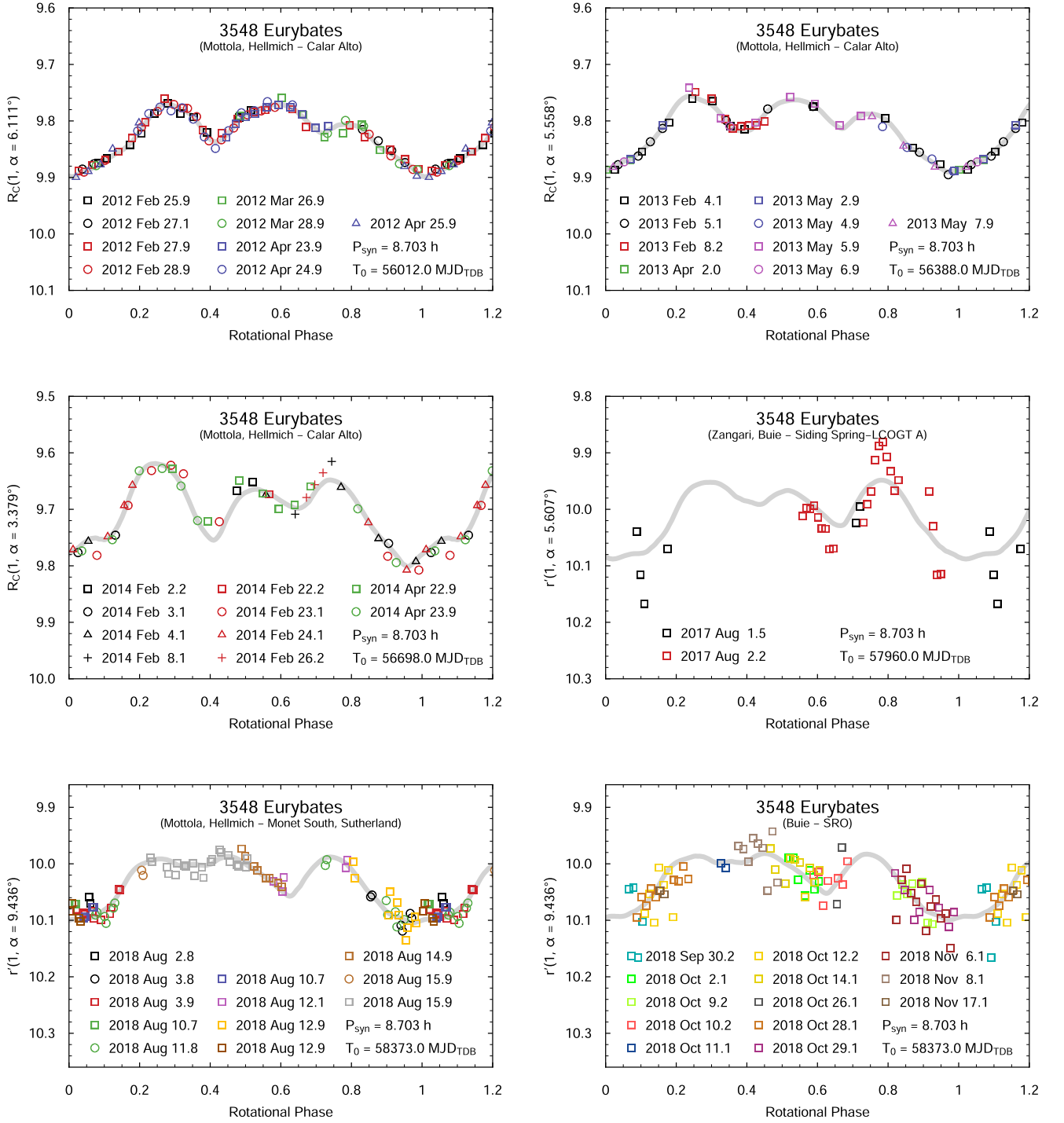
For the convex inversion of Eurybates we used new and historical data for a total of 1960 photometric data points spanning a period of 29.6 yr. Although the new data presented here already allow a reliable solution to be determined, the additional historical and sparse data enable a more accurate period determination and the application of direct facet-area inversion, as explained in Section 3.4. Figures 1 and 2 show selected light-curve data for Eurybates during different apparitions. Given the small variation of the illumination and viewing angles during each apparition—and the consequent small intra-apparition variation of the shape of the light curves—all the data for a particular year have been composited together for a given observing station, with the respective best-fit synodic period. The composites show asymmetric light curves, characterized by a small amplitude during most apparitions and by three pairs of extrema. Observations during the 2017 apparition occurred when Eurybates’s apparent location was close to the galactic center. For this reason, those observations show larger residuals and systematics that are due to imperfect star subtraction. These observations have been weighted accordingly in the inversion.

### 4.2. Colors and Color Variations

In 2020 October Eurybates was observed with a high cadence from Calar Alto in the *BRI* Johnson–Cousins photometric bands for four consecutive nights in order to assess the presence of possible color variegation over the surface. Occasionally, frames were acquired in the Johnson *V* filter to determine the corresponding color indices. The four nights were of photometric quality, and the resulting time series covered more than three Eurybates complete rotations, with a typical S/N for the individual measurements ranging from 125 for the *B*-filter exposures to 280 for the *R*-filter ones. The light curves in the *R* filter—the ones with the highest accuracy—were fitted with a 14th-order Fourier polynomial, in order to provide the baseline against which the time-resolved color indices were computed. The results are presented in Figure 3. The top panel shows the *R*-band light curve along with the Fourier-series fit, while the second panel from the top shows the *R*-band residuals to the fit. The rms of the residuals in the *R* band is  $\sigma = 0.0045$  mag, which is quite compatible with the S/N of the measurements, showing both the adequacy of the chosen fit order and the good reproducibility of the measurements across the four nights of observation. The third and fourth panels from the top represent the *B* – *R* and *R* – *I* color indices, computed by subtracting the *R*-band Fourier fit from the *B* and *I* magnitudes, respectively. The rotationally averaged *B* – *V*, *V* – *R*, and *R* – *I* color indices are reported in Table 3.

Figure 3 shows that no systematic, repeated color variations are detected for Eurybates in the observed bands. A fit to the residuals produces curves with an amplitude smaller than 0.01 mag. To give some context, the hemispherical color-index variations for (4) Vesta for the bands 954–720 nm (comparable to the *I* – *R* index) amount to about 6% (Jaumann et al. 1996).

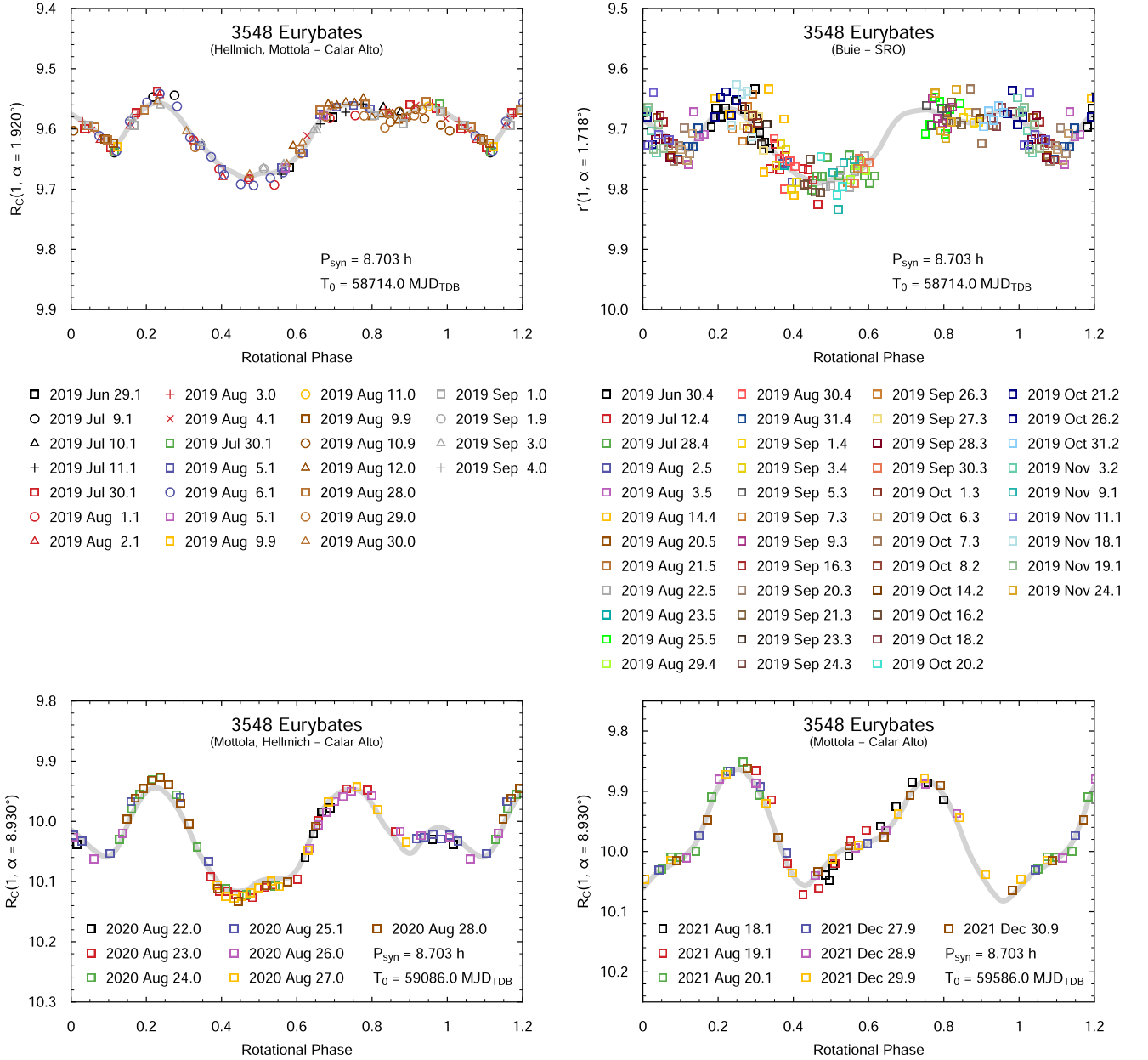
The observations were carried out close to exact opposition, with nearly a complete rotation observed during each night. Furthermore, at the time of the observations the object presented the observer with a near-equatorial aspect, with a subobserver latitude of about  $-18^\circ$  (see Section 4.3). From this



**Figure 1.** Composite light curves of Eurybates for the period 2012–2018. The data points beyond rotational phase 1.0 are repeated for clarity.  $P_{\text{syn}}$  is the exact value of the synodic period used for folding the light curves, and as such, it is quoted without error. The reference epoch  $T_0$  is one-leg light-time corrected and expressed in the TDB uniform frame. The magnitudes are reduced to the distance of 1 au from the Sun and from the observer. A small correction is applied to the magnitudes to reduce them to the reference phase angle of each observation set, shown in the respective y-axis label. Each symbol corresponds to an individual night of observation, centered at the UT epoch listed in the label. Observations on different nights reported with the same color have been reduced with the same set of catalog stars and are therefore tied in an absolute way. Observations reported in different colors have been performed with different sets of catalog stars and have been arbitrarily shifted in magnitude to account for catalog uncertainties. The applied shifts are typically smaller than 0.01 mag. The solid gray curve is the synthetic light curve obtained for the respective  $T_0$  epoch with the best-fit shape model and photometric parameters (see text).

observation geometry, most of the object’s surface ( $\geq 97\%$ ) is exposed to the observer during one rotation. As a consequence, we conclude that no major global-scale color variegation is present on Eurybates in the observed bands, although small-

scale color heterogeneity might still exist. In addition, the measurements performed are not diagnostic for spectrum-neutral albedo variations, which, although unlikely, might be present even on a global scale.



**Figure 2.** Composite light curves of Eurybates for the period 2019–2020. Notation is the same as in Figure 1.

#### 4.3. Sidereal Period, Pole, and Shape

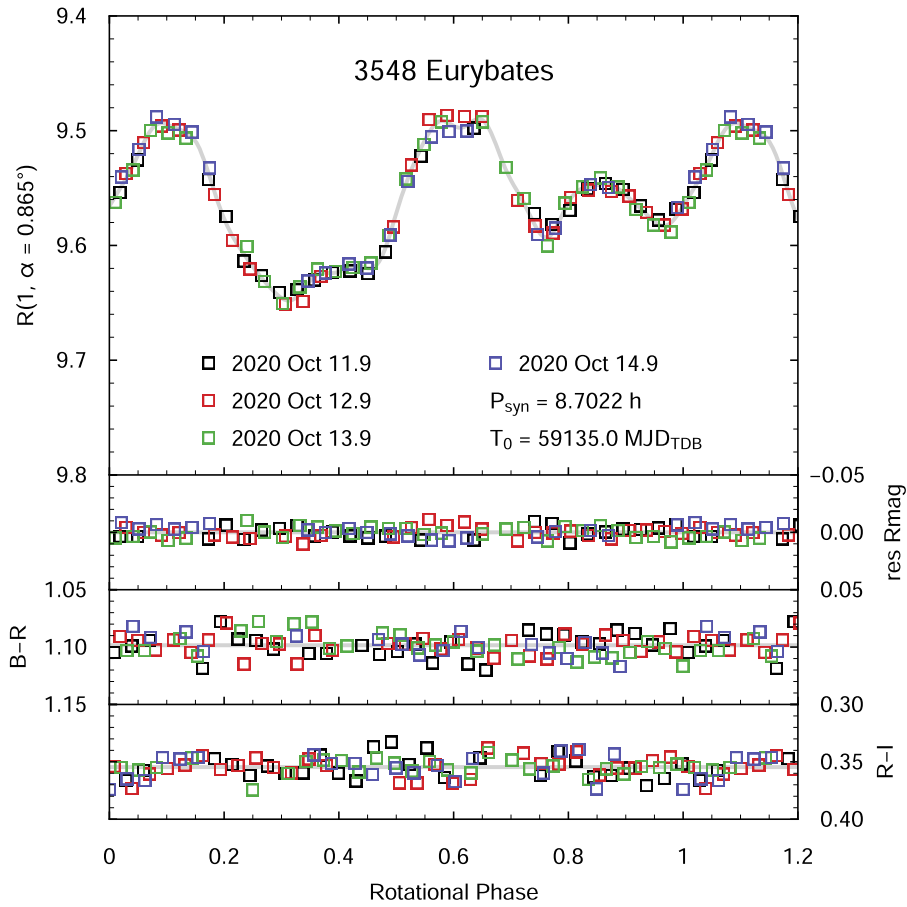
The sidereal period for Eurybates was searched for by performing about 21,000 full convex inversion runs on the whole data set using, as initial conditions, 12 different pole directions, equally spaced on the celestial sphere, and a series of trial periods densely covering the range of possible period solutions. All shape, photometric, and rotation parameters (including the rotation period) were optimized. The resulting period scan (see Figure 4) shows an unequivocal global minimum at  $P_{\text{sid}} = 8.7027283 \pm 0.0000029 \text{ h}$ , thereby confirming and improving on the previous sidereal period determinations mentioned in the introduction. This best-fit sidereal period was used as starting value for the  $\chi^2$  map in Figure 5, which was generated by running the shape inversion procedure for about 20,000 fixed discrete directions on the celestial sphere, while simultaneously solving for sidereal period, shape, and photometric properties. For the generation of the  $\chi^2$  map the

EGI was approximated with a spherical harmonics polynomial of degree and order 6 sampled with a Lebedev rule of order 302 (Lebedev & Laikov 1999; Kaasalainen et al. 2012).

The  $\chi^2$  map shows the presence of two equally likely retrograde solutions characterized by an ecliptic longitude difference of about  $180^\circ$ . This fundamental phenomenon is known as the *longitude ambiguity* (Kaasalainen & Lamberg 2006) and occurs whenever unresolved measurements are confined to a geometry (defined by the Sun, observer, and target) close to the same plane for all of the observations. In this case this condition occurs because, due to its orbital inclination, the geocentric ecliptic latitude of Eurybates never exceeds  $\pm 10^\circ$ .

Keeney et al. (2021), as a part of their program for the determination of size and shapes of the Lucy targets via stellar occultations (Buie et al. 2021), have reported their preliminary results about a Eurybates event recorded on 2021 October 20.5





**Figure 3.** Time-resolved color observations of Eurybates during the 2020 apparition. The top panel shows the  $R$ -band light curve along with the corresponding Fourier fit. The second panel from the top shows the  $R$ -band residuals to the fit, while the third and fourth panel show the  $B - R$  and  $R - I$  time-resolved color indices, respectively. See text for details.

UT with nine usable chords. By projecting the shape models corresponding to our two solutions onto the plane of the sky at the time of the occultations and by overplotting the occultation chords, it was possible to unambiguously identify the correct pole solution, which is marked in Figure 5 with a red circle.

The obliquity of the spin axis with respect to its orbital pole is about  $158^\circ$ , which makes Eurybates experience only moderate seasonal variations along its orbit.

The final convex shape model has been computed by direct inversion of the facet areas of a polyhedron with 1454 polygonal facets, as detailed in Section 3.4. The corresponding synthetic light curves are plotted as gray solid curves in Figures 1 and 2, showing that the model follows the observed light curves down to the data scatter. The deviation from a perfectly closed convex shape (Kaasalainen & Torppa 2001) is a small 0.11% of the total surface, encouraged through a mild regularization coefficient. This small residual, often referred to as a dark facet, implies that the observed light curves can be satisfactorily explained by a convex shape with uniform albedo, and hemispherical-scale albedo variations are not required. The geometric principal axis of inertia of the convex shape computed by assuming constant bulk density is tilted by about  $8^\circ$  from the spin axis. This deviation could be a hint that the object displays some degree of nonconvexity and/or its density distribution is not uniform.

Figure 6 shows three different views of the best-fit convex shape model of Eurybates. The body has an irregular shape

with a moderate elongation, with axial ratios reported in Table 3.

The availability of occultation data also allowed us to fix the absolute scale of the model, by minimizing the Euclidean distances of the occultation transition points and the projection of the shape model at the time of the event (see Mottola et al. 2020). Figure 7 shows the occulting silhouette of Eurybates at the time of the 2021 October 20 event, along with the recorded chords. The model corresponding to the rejected pole solution is overplotted in gray for comparison. The size of the red circles roughly corresponds to the uncertainty on the timing of the ingress or egress events. Considering that the occultation data have not been used in the determination of the rotation and shape models (other than resizing), we regard the match with the occultation chords as remarkable, although hints of nonconvexities are present.

#### 4.4. Photometric Properties

In addition to performing the convex inversion for Eurybates with the  $H$ ,  $G_1$ ,  $G_2$  surface phase function, we also used the linear exponential function, for the purpose of comparison. The respective best-fit parameters are shown in Table 3, while Figure 8 shows the sphere-integrated phase curve. This representation leverages the known shape model and observation geometry to remove the effects on the phase curve due to varying rotation phase and aspect angle during different apparitions. The result corresponds to the phase curve of a

**Table 3**  
Results

	Eurybates	Orus
Sidereal period (h)	$8.7027283 \pm 0.0000029$	$13.486190 \pm 0.000017$
Pole ecl. long., lat. (deg J2000)	320, -60	33, -59
Pole R.A., decl. (deg J2000)	7, -67	54, -42
Error ellipse <sup>a</sup> of pole coords. (deg, $1\sigma$ )	3, 5	3, 5
Ecliptic obliquity of pole (deg)	150	149
Orbital obliquity of pole (deg)	158	154
$T_0$ (JD <sub>TDB</sub> )	2,448,765.0	2,455,116.0
$\Phi_0$ (deg)	65.418	60.854
$W_0$ (deg)	229.156	17.413
$\dot{W}$ (deg day <sup>-1</sup> )	$992.79211 \pm 0.00033$	$640.65535 \pm 0.00081$
$A_0$	$0.55 \pm 0.04$	$0.41 \pm 0.06$
$D$ (rad)	$0.133 \pm 0.005$	$0.143 \pm 0.014$
$k$ (rad <sup>-1</sup> )	$-1.16 \pm 0.04$	$-0.89 \pm 0.08$
$c$ (fixed)	0.1	0.1
$H_{V\text{-linexp}}$ (sph. int.)	$9.854 \pm 0.005$	$10.241 \pm 0.007$
$H_{V\text{-}H,G_1,G_2}$ (sph. int.)	$9.800 \pm 0.007$	$10.204 \pm 0.006$
$G_1$	$0.862 \pm 0.019$	$0.689 \pm 0.012$
$G_2$	$-0.028 \pm 0.011$	$0.193 \pm 0.007$
$p_V$ (lin-exp)	$0.042 \pm 0.003$	$0.039 \pm 0.002$
$p_V$ ( $H, G_1, G_2$ )	$0.044 \pm 0.003$	$0.040 \pm 0.002$
$B - V$	$0.739 \pm 0.026$	$0.799 \pm 0.031$
$V - R$	$0.384 \pm 0.021$	$0.454 \pm 0.021$
$R - I$	$0.355 \pm 0.015$	...
$L_X$ (km)	77.5	70.7
$L_Y$ (km)	71.3	63.0
$L_Z$ (km)	61.8	51.4
$L_X/L_Y$	1.09	1.12
$L_Y/L_Z$	1.15	1.23
Surface-equiv. spherical diam. (km)	$69.3 \pm 1.4$	$60.5 \pm 0.9$
Photometric surface (km <sup>2</sup> )	$1.51 \times 10^4$	$1.10 \times 10^4$
Convex shape volume (km <sup>3</sup> )	$1.67 \times 10^5$	$1.13 \times 10^5$

**Notes.** Please refer to the text and to Mottola et al. (2020) for the definition of the respective quantities.

<sup>a</sup> Semiaxes of the error ellipse projected onto the sky plane for the ecliptic longitude and latitude directions, respectively.

hypothetical spherical object with the same regolith photometric properties as the target (Mottola et al. 2020). For this reason, the scatter in the individual data points (blue squares) is almost entirely due to the measurement noise, and not to the varying observation geometry. This representation also highlights the very high accuracy of the absolute photometry of our measurements, which is mainly due to two factors. First, the absolute measurements used for the phase curve have been acquired with the same telescope/instrument/filter combination over the whole decade spanned by the observations, which provides for good internal consistency. Second, the accuracy and consistency of the Gaia photometric catalog, the large field of view of the camera containing a large number of in-field catalog stars, and the availability of accurate transformations between the Gaia and the Johnson photometric systems

(Evans et al. 2018) allowed for reliable absolute-magnitude determinations over the whole sky.

The phase curve covers the range  $0^\circ\text{--}12^\circ\text{.3}$  in solar phase angle and shows a nearly linear trend with a very subdued opposition effect, as already observed for other Trojan asteroids (Shevchenko et al. 2012; Buie et al. 2018; Mottola et al. 2020). The magnitude difference between  $1^\circ$  and  $11^\circ$  solar phase is  $\Delta M_{(1^\circ, 11^\circ)} = -0.548$ . Within the observed range the  $H$ ,  $G_1$ ,  $G_2$  and the linear exponential fits produce accurate, virtually indistinguishable results. On the other hand, the old HG system—a fit to which is also shown in Figure 8 for reference—shows systematic deviations and fails to reproduce the nearly linear trend of the data.

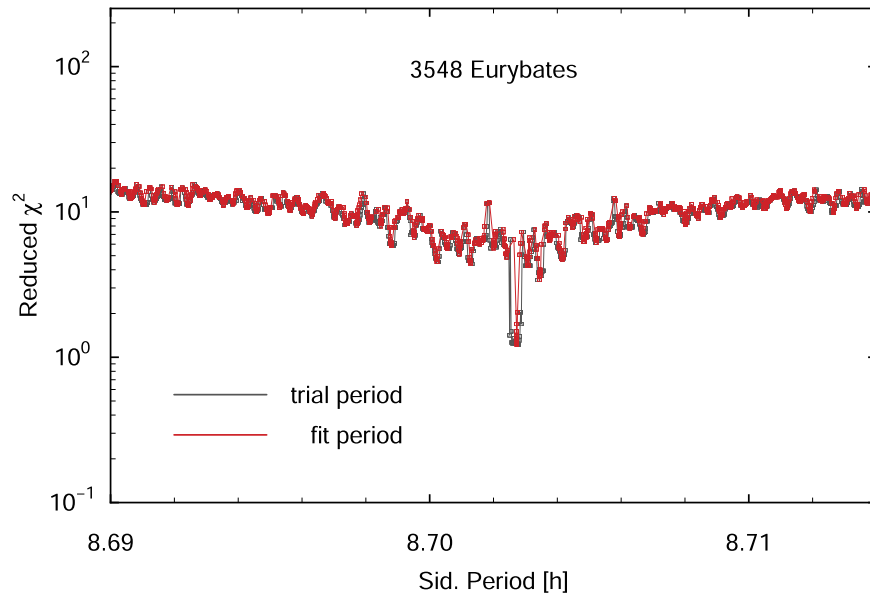
In the phase-angle range  $\leq 0^\circ\text{.8}$ —unconstrained by the data—the linear exponential and the  $H$ ,  $G_1$ ,  $G_2$  functions conduce to different results, which, in turn, produces the two slightly different  $H$  and  $p_V$  sets of values reported in Table 3 for the two photometric systems. These differences have virtually no effect for nearly all practical applications, as long as those  $H$ -values are used in conjunction with the respective phase functions. This effect highlights the importance of always specifying the function used to extrapolate the observations to zero phase.

Analyzing our phase curve with the unsupervised  $H$ ,  $G_1$ ,  $G_2$ , the unidimensional classification tool by Penttilä et al. (2016) assigns Eurybates to the taxonomic type C, solely based on the shape of the phase curve, thereby independently confirming the classification by Fornasier et al. (2007) based on visible spectroscopy. This independent confirmation is particularly important, given the scarcity of C-type objects present in the Trojan clouds.

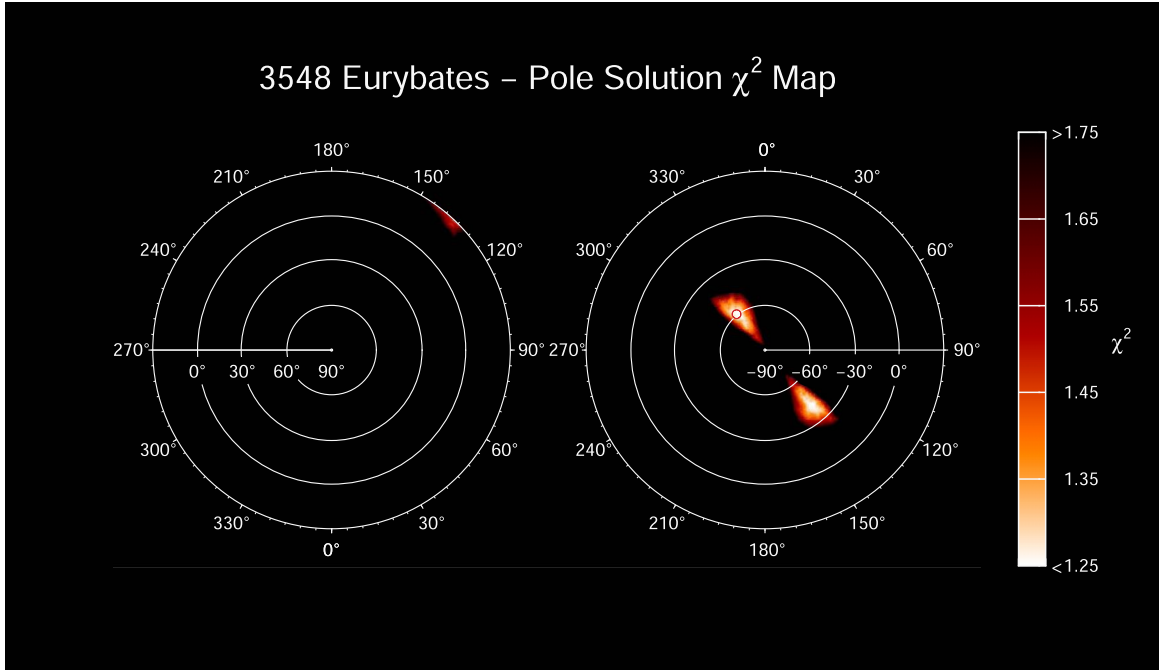
#### 4.5. Size and Albedo

In addition to breaking the longitude ambiguity of the pole solutions, the stellar occultation measurements by Keeney et al. (2021) also fix the absolute scale of our shape model and, in conjunction with our absolute-magnitude determination, its geometric albedo. The spherical-equivalent diameter is  $D_s = 69.3 \pm 1.4$  km, where the error has been determined by estimating the uncertainty of the cross-sectional area at the time of the occultation event at 4% and the influence of the uncertainties from the other parameters by using the bootstrap method. In Table 3 we report the values of  $p_V$  obtained for both the linear exponential and  $H$ ,  $G_1$ ,  $G_2$  photometric systems. The albedo determination by Grav et al. (2012) mentioned in the introduction ( $p_V = 0.052 \pm 0.007$ ) is compatible with our own, with the error bars of the respective measurements marginally overlapping. The determinations by Tedesco et al. (2004) and Usui et al. (2011), on the other hand, are both considerably brighter than our occultation-derived value. The reason for that, however, can be easily traced back to the literature  $H$ -value used in the last two works ( $H = 9.50$ ), which overestimates the object's brightness. Adopting our value for  $H$  and recomputing the albedo with the method proposed by Harris & Harris (1997) resolves the discrepancy.

The size determinations by Tedesco et al. (2004) and Usui et al. (2011) are compatible with our own, within the respective error bars, while Grav's diameter is about 8% smaller than our value.



**Figure 4.** Sidereal period scan for Eurybates. Trial periods correspond to the start values for each individual optimization run, while fit periods are the resulting optimized values.



**Figure 5.** Polar azimuthal equidistant projection of the  $\chi^2$  of the pole solutions for Eurybates. The coordinates are expressed in the J2000 ecliptic frame. The left panel is centered on the north ecliptic pole and the right one on the south ecliptic pole. The equatorial region (ecliptic latitudes  $-30^\circ$  to  $+30^\circ$ ) is mapped in both panels. The loci of the two complementary best solutions are clearly visible as white regions. The red circle marks the correct solution identified through its match with the stellar occultation chords by Keeney et al. (2021).

## 5. Orus

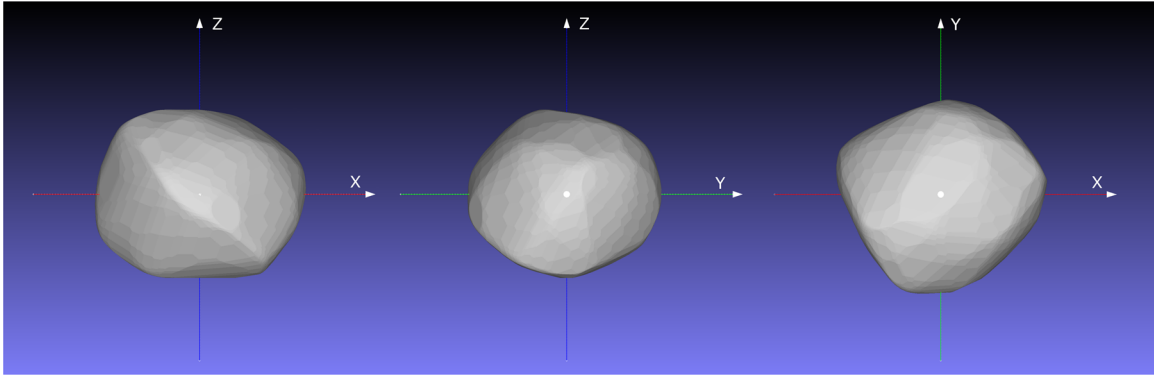
### 5.1. Light Curves

The photometric data set used for the inversion of Orus consists of a total of 3082 data points encompassing a time span of 12.2 yr. Figures 9 and 10 show selected composite light curves for Orus during various apparitions. The composites show asymmetric two-maxima, two-minima light curves during most apparitions, with a less pronounced and broader secondary maximum. The observed maximum amplitude of

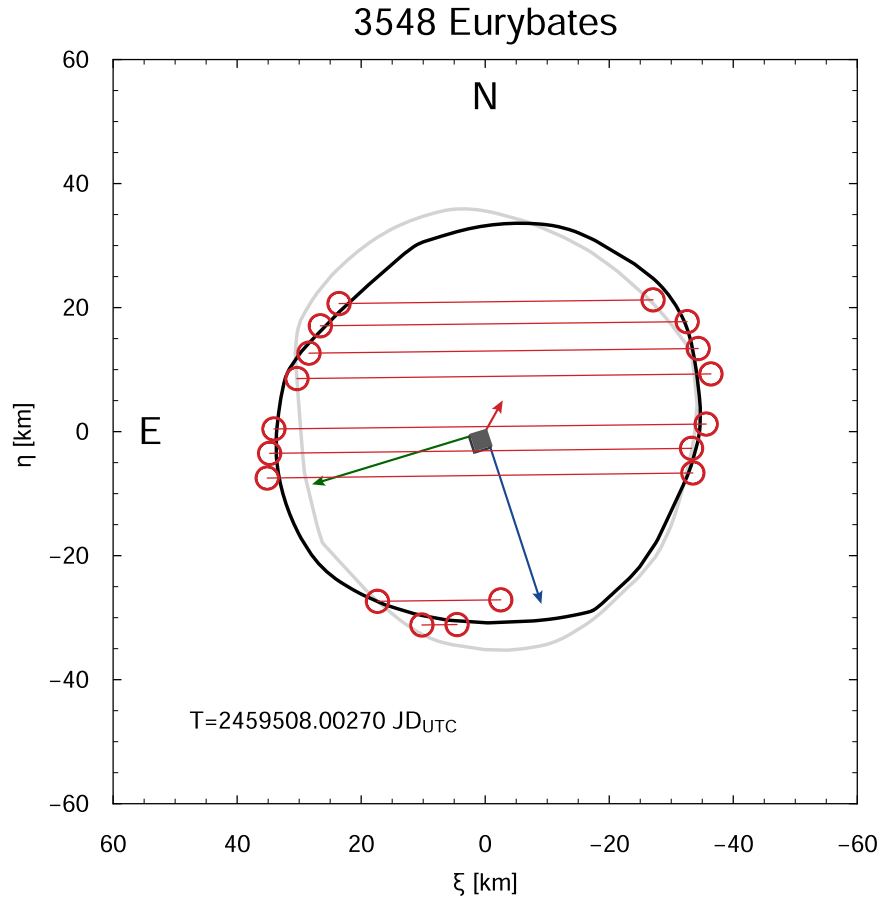
0.23 mag occurred during the 2017 apparition, while the minimum amplitude of 0.17 mag was registered in 2019.

### 5.2. Colors and Color Variations

In 2020 August Orus was observed at high cadence with the Johnson–Cousins filters *BVR* for five consecutive nights, in order to assess its color heterogeneity over the surface, as described earlier for Eurybates. Unfortunately, differently from the Eurybates case, at the time of observation the *I* filter was not



**Figure 6.** Three orthographic views of the Eurybates convex shape model.



**Figure 7.** Occulting silhouettes of the best-fit convex model of Eurybates (solid black line) along with the rejected complementary model (displayed in light gray) at the time of the 2021 October 20 occultation. The red, green, and blue arrows represent the  $X$ -,  $Y$ -, and  $Z$ -axes in the body-fixed reference frame, respectively.

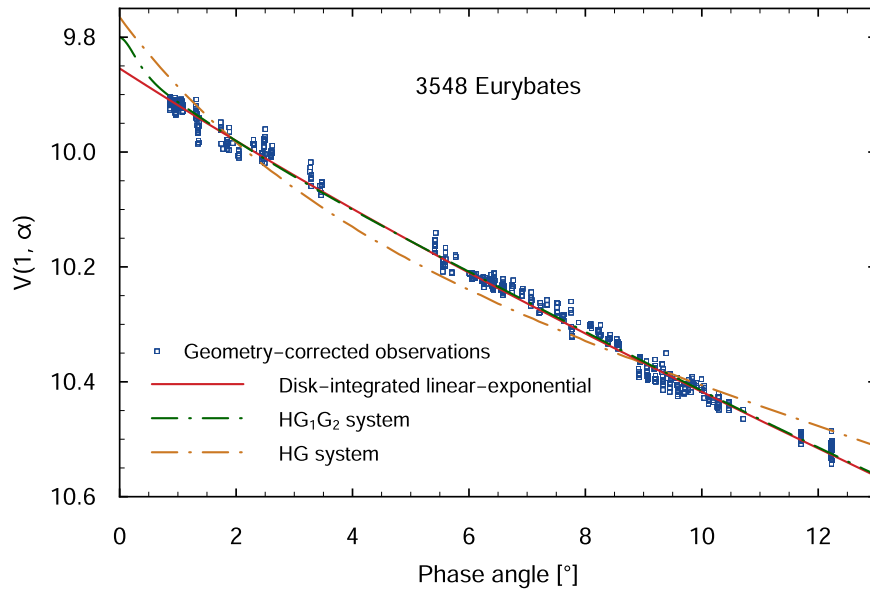
available at the telescope, thereby limiting somewhat the monitored spectral range. The subobserver latitude of Orus at the time of the observations was  $-16^\circ$ , implying a viewing aspect close to equatorial, with most of the surface being observed during a rotation. The five nights of observation, all of photometric quality, enabled us to cover the 13.5 h rotation period twice, providing for confirmation in case of the detection of a color variation. Typical S/N levels for the individual exposures ranged from 80 in the  $B$  band to 200 in the  $R$  filter—somewhat lower than in the case of Eurybates, due to the lower apparent brightness of Orus. The light curve in the  $R$  filter was fitted with a 15th-order Fourier polynomial (shown in Figure 11 as a gray solid curve) and used as a baseline for subtracting the observations in the other

filters, thereby obtaining the time-resolved  $B-R$  and  $V-R$  indices shown in the third and fourth panels from the top in Figure 11. The residuals in the  $R$  band, shown in the second panel from the top in Figure 11, have an rms value  $\sigma = 0.0065$  mag. Again, as in the case of Eurybates, no systematic, repeated color variations are detected for Orus, which excludes global-scale spectral variations over the observed spectral range, although local variations remain possible. The rotationally averaged  $B-V$  and  $V-R$  color indices are reported in Table 3.

### 5.3. Sidereal Period, Pole, and Shape

The period scan for Orus (Figure 12) was obtained by performing about 30,000 full inversions starting from 12





**Figure 8.** Sphere-integrated phase curve for Eurybates. The blue squares represent the geometry-corrected individual data points for the subset of the observations for which a reliable transformation to the Johnson V band could be determined.

discrete pole directions and from initial sidereal periods densely covering the range of possible solutions. The scan shows a well-defined global minimum at a sidereal period  $P_{\text{sid}} = 13.486190 \pm 0.000017$  h. A secondary side minimum is also present that corresponds to a  $\chi^2$  larger by about 50% than the primary minimum. This spurious solution corresponds to a model in which the primary and secondary light-curve maxima are swapped for some of the observations.

As in the case of Eurybates, the  $\chi^2$  map in Figure 13 shows the presence of two indistinguishable, retrograde, equally probable solutions for the spin axis vector, which is due again to the  $180^\circ$  longitude ambiguity, given the low orbital inclination of the object and the consequent small range of geocentric ecliptic latitudes ( $\pm 10^\circ$ ) at which the object was observable.

Keeney et al. (2021) report results about an Orus stellar occultation event recorded on 2021 October 16.1 UT in Senegal. Preliminary reduction of the occultation data resulted in six positive chords and a close-miss negative detection for this event. The location of the chords is compatible with our Solution 1, marked with a red circle in Figure 13, and excludes Solution 2, thereby resolving the pole ambiguity.

The obliquity of the spin axis with respect to its orbital pole is  $154^\circ$ , making Orus, similarly to Eurybates, an object with a moderate seasonal cycle.

The final model shape has been computed by direct inversion of the facet areas of a polyhedron with 2354 facets, as detailed in Section 3.4. The resulting synthetic light curves are reported as solid gray lines in Figures 9 and 10.

The convexity residual is low, at 0.2% of the total surface, showing that also in the case of Orus hemispherical-scale albedo variations are not required to explain the observed light curves.

The tilt of the principal axis of inertia of the convex shape with respect to the spin axis is about  $3^\circ$ . Considering that the convex shape is a photometric and not dynamical representation of the body and that the principal axis of inertia is totally unconstrained during the optimization, the alignment of the two axes is very good.

Figure 14 shows different views of the Orus convex shape model. The body has an irregular shape with a moderate elongation. The extent of the body along its axes (see Mottola et al. 2020 for definition), along with its axial ratios, is reported in Table 3.

As in the case of Eurybates, the availability of occultation data also allowed us to fix the absolute scale of the Orus model. Figure 15 shows the occulting silhouette of Orus at the time of the 2021 October 16 event, along with the recorded chords. The model corresponding to the rejected pole solution is overplotted in gray for comparison. Also in this case, the match with the occultation chords is very good. No hints of a major nonconvexity are seen in this observation geometry.

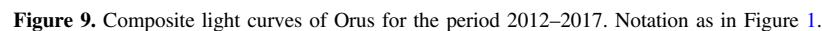
#### 5.4. Photometric Properties

The best-fit photometric parameters for Orus are shown in Table 3, while Figure 16 shows its sphere-integrated phase curve. The phase curve covers the range  $0.5^\circ$ – $11^\circ$  and, with a  $\Delta M_{(1^\circ;11^\circ)} = -0.428$ , is shallower than Eurybates's in the observed phase-angle range. As in the case of Eurybates, the curve is nearly linear and lacks a pronounced opposition effect, with both the linear exponential and the  $H$ ,  $G_1$ ,  $G_2$  functions resulting in near-identical fits reproducing the trend with high fidelity. The two functions only split in the unconstrained phase-angle range below  $0.5^\circ$ . Again, the HG system function fails to reproduce the linear behavior of the curve.

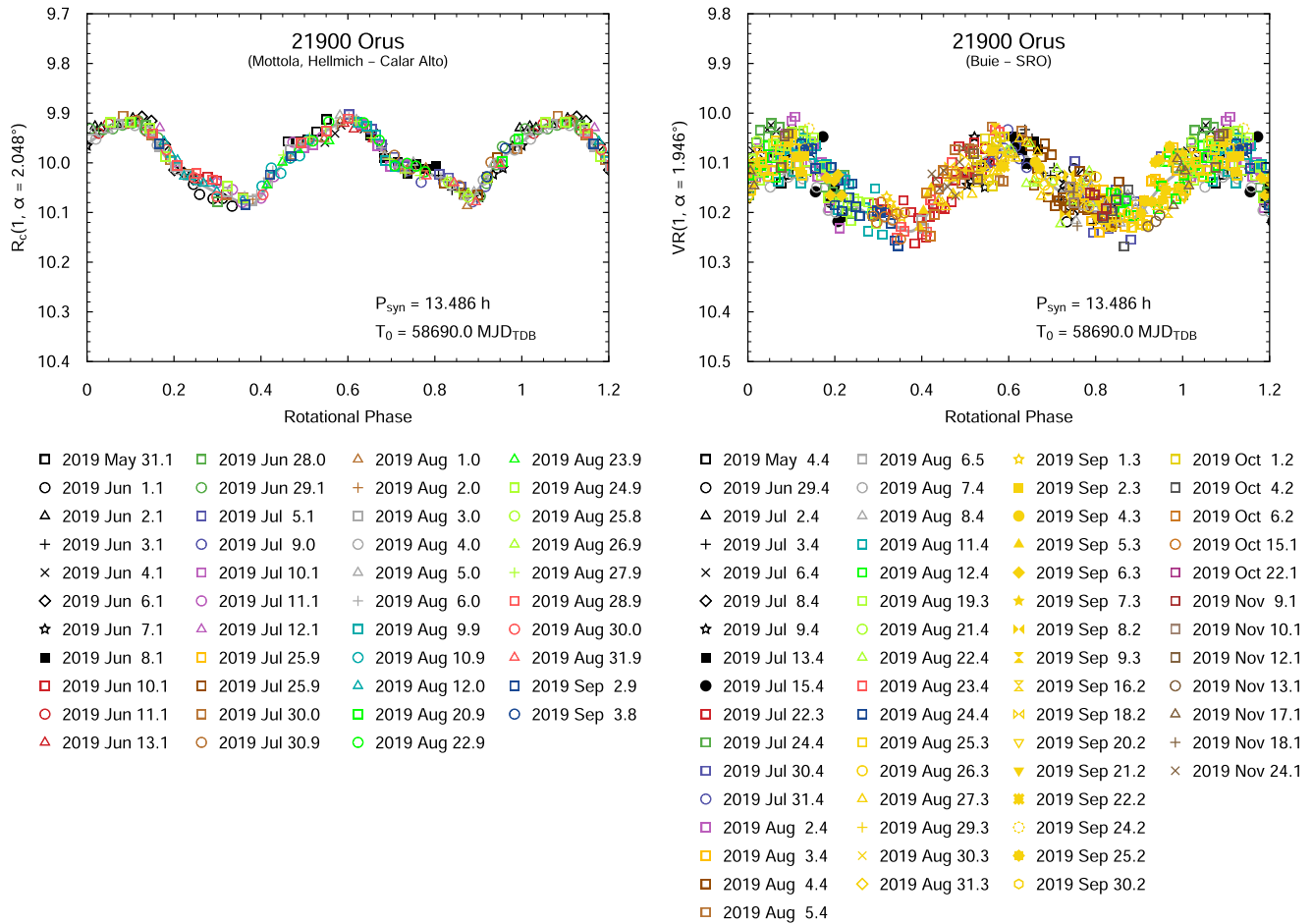
The tool by Penttilä et al. (2016) applied to the Orus phase curve assigns the object to the taxonomic type D, which supports the previous classification based on NIR spectra.

#### 5.5. Size and Albedo

By rescaling our Orus shape model to match the observed occultation chords by Keeney et al. (2021), we obtain a spherical-equivalent diameter  $D_s = 60.5 \pm 0.9$  km and geometric albedo values of  $p_V = 0.039 \pm 0.002$  in the case of the linear exponential surface phase function and  $p_V = 0.040 \pm 0.002$  in the case of the  $H$ ,  $G_1$ ,  $G_2$  function. Our new determinations differ considerably from those of Grav et al. (2012) and



the object brightness by a large amount with respect to our best-fit  $H$ -value in the HG system. By using our own determination for  $H$  and applying the method by Harris & Harris (1997) to recalculate Grav’s and Usui’s geometric albedos, we obtain  $p_V = 0.060$  for both cases, which, although reducing the gap, is



**Figure 10.** Composite light curves of Orus for the 2019 apparition. Notation as in Figure 1.

still an overestimation. We conclude that, in addition to an incorrect  $H$ -value, the radiometric determinations and/or the thermal modeling for Orus by Grav et al. (2012) and Usui et al. (2011) are affected by systematics that exceed by far the quoted uncertainties.

## 6. Discussion and Conclusions

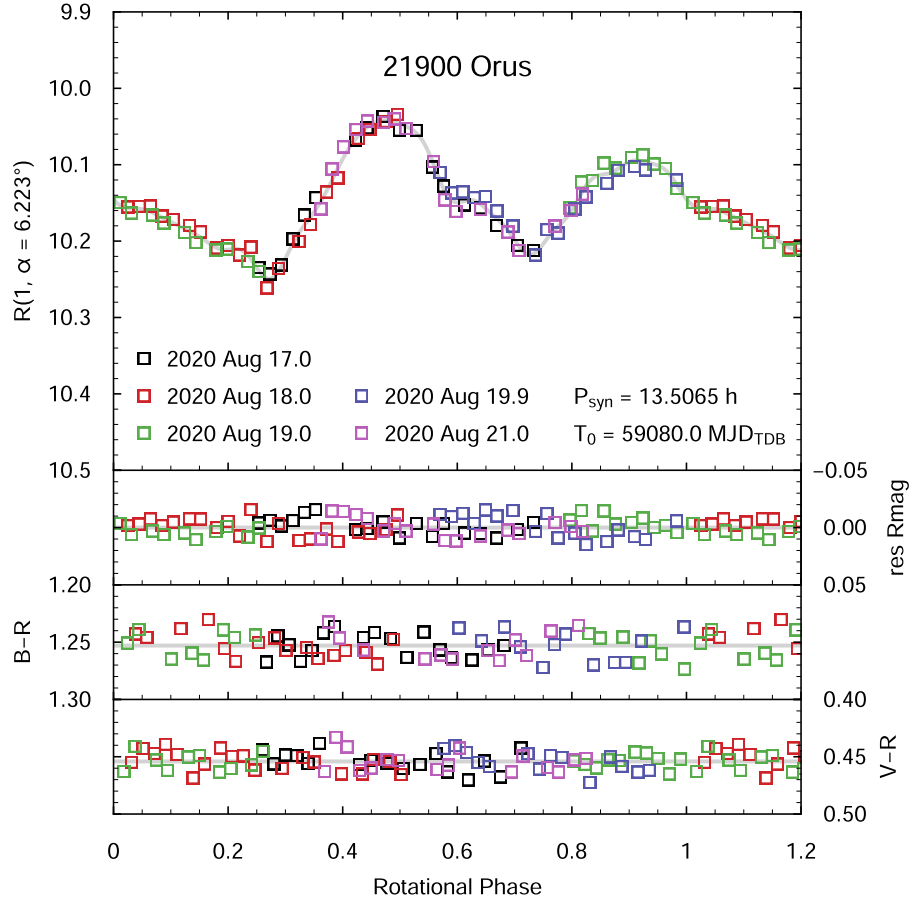
We have collected new, accurate light-curve observations over the past decade that cover nearly one complete revolution of the targets around the Sun and combined them with historical observations to determine photometric properties and rotation and convex shape models for two of the Lucy mission targets. We have introduced a surface phase function that, in combination with the Lommel–Seeliger–Lambert disk function, allows direct inversion of the  $H$ ,  $G_1$ ,  $G_2$  parameters. The advantage of this formalism is that the description of the photometric properties is made directly in a standard IAU photometric system, which allows for simple comparison with literature results and holds the potential for a photometry-based taxonomic classification. Further, we have introduced the concept of semi-absolute photometry, which enables full exploitation of absolute photometry information in the convex inversion of light curves, regardless of the degree of accuracy, and have applied several other improvements that have increased the accuracy, efficiency, and stability of the convex inversion scheme.

Matching our shape models with stellar occultation chords by Keeney et al. (2021) has resolved the longitude ambiguity of the pole directions of Eurybates and Orus, has fixed their absolute size, and has allowed us to determine their geometric albedo.

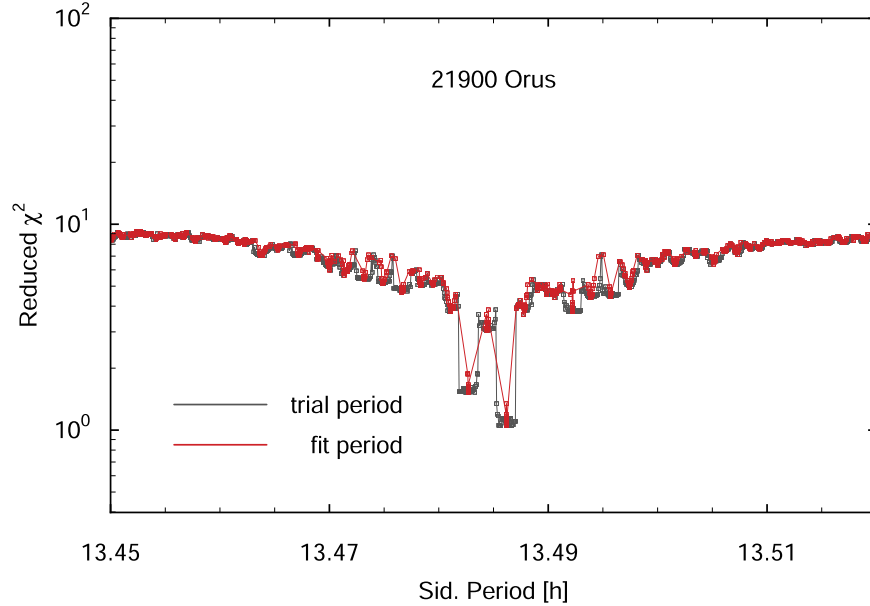
Both Eurybates and Orus are low-elongation, irregular bodies for which the derived convex shape model can reproduce all of the observed light curves down to the scatter of the data points. This condition, however, is not sufficient to exclude the presence of even large concavities because disk-integrated light curves acquired at small phase angles (as unavoidable for distant objects) carry little or no information about nonconvex features (Durech & Kaasalainen 2003). The use of complementary techniques, as stellar occultation observations, will be fundamental in establishing the presence of possible significant deviations from convexity. A major observational effort has been initiated to that end with the aim of retrieving dense chord coverage for all of the Lucy targets (Buie et al. 2020).

Noll et al. (2020) reported the discovery of Queta, a satellite orbiting Eurybates—a likely testimony to its intense collisional past. With a size of about  $\sim 1$  km, however, this satellite is too small to imprint a detectable signature on our light curves. Similarly, we did not observe in the light curves any hint of a possible, still-undetected further companion—neither for Eurybates nor for Orus.

With very low convexity residuals, the shape models for both objects do not suggest the presence of strong, global-scale



**Figure 11.** Time-resolved color observations of Orus during the 2020 apparition. The top panel shows the  $R$ -band light curve along with the corresponding Fourier fit. The second panel from the top shows the  $R$ -band residuals to the fit, while the third and fourth panels show the  $B - R$  and  $V - R$  time-resolved color indices, respectively. See text for details.



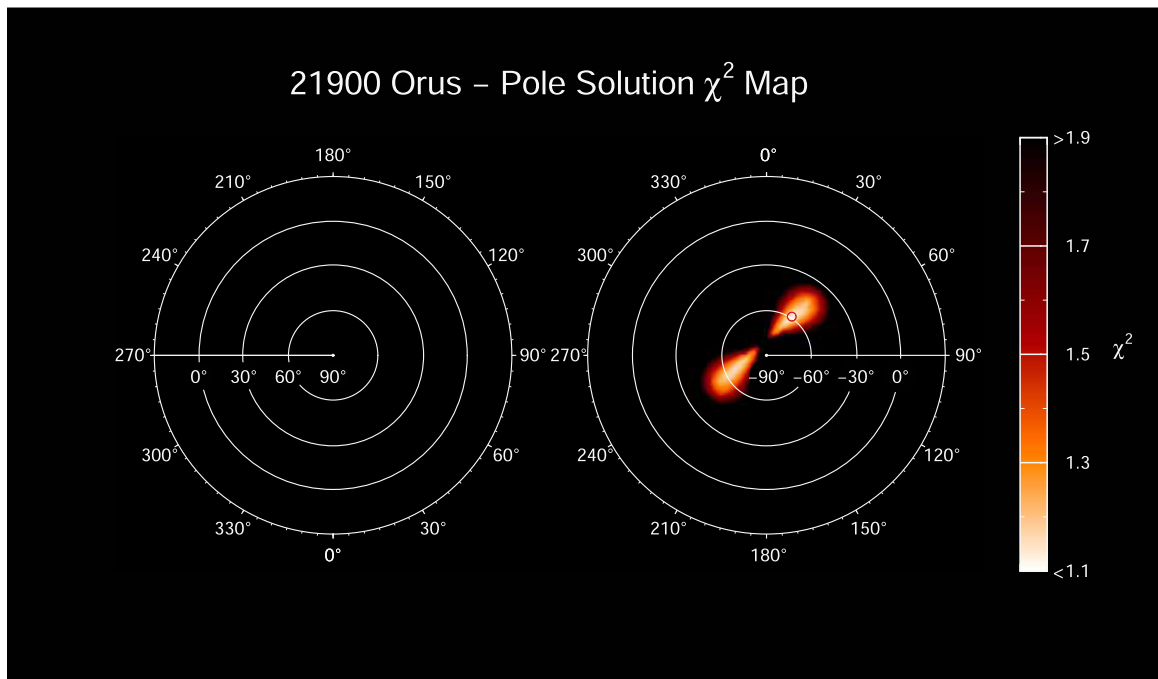
**Figure 12.** Sidereal period scan for Orus.

albedo contrast. In addition, our time-resolved, repeated color observations in several spectral bands have not revealed hemispheric-scale variegation in the visible range larger than 1%. These observations seem to refute previously reported putative large spectral slope variations for Eurybates

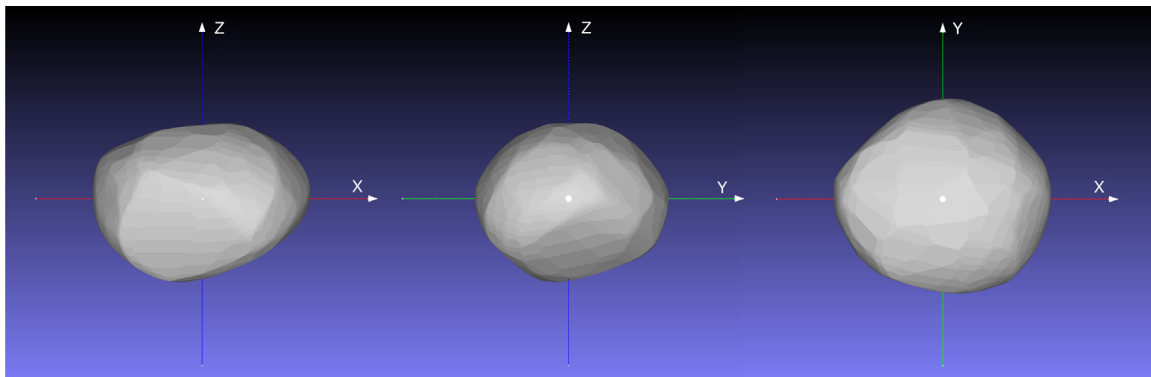
(Souza-Feliciano et al. 2020). However, it is still possible that the objects could display albedo or color contrast at scales that are small with respect to their diameter.

The unsupervised classification tool by Penttilä et al. (2016) identifies Eurybates as a C type and Orus as a D type based on





**Figure 13.** Same as Figure 5, but for Orus.



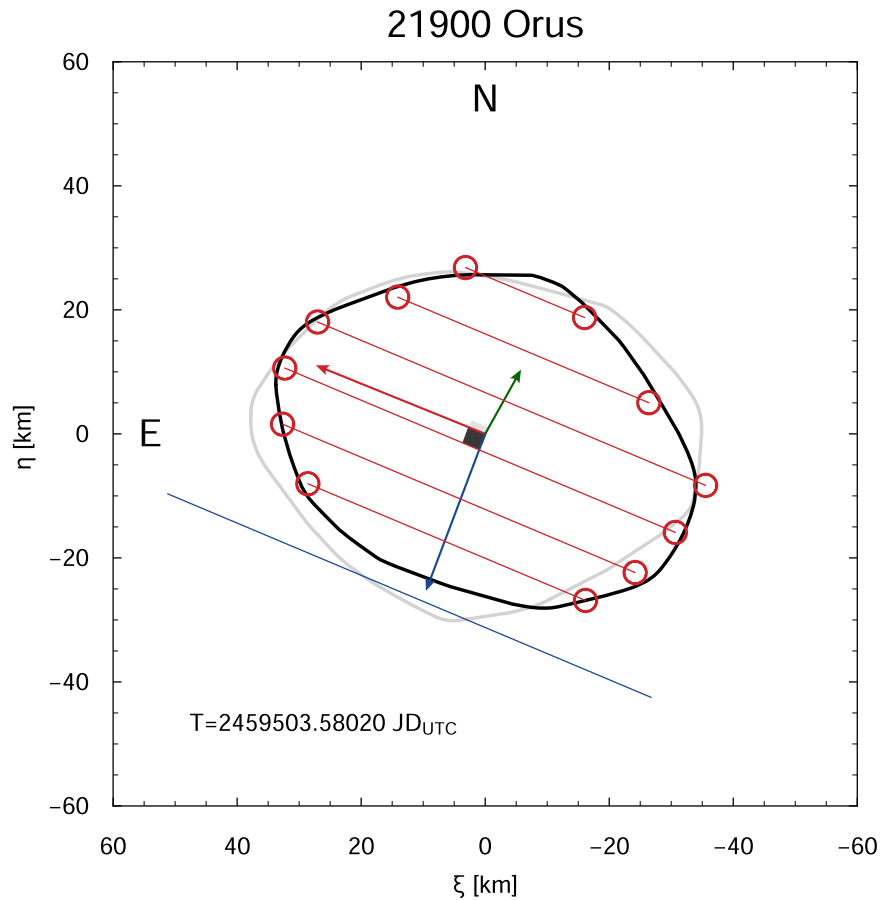
**Figure 14.** Three orthographic views of the Orus convex shape model.

photometry alone, thereby independently supporting current taxonomic memberships based on NIR spectroscopy. Especially for Eurybates this is an important confirmation, as the C taxonomic type is quite rare in the Trojan region.

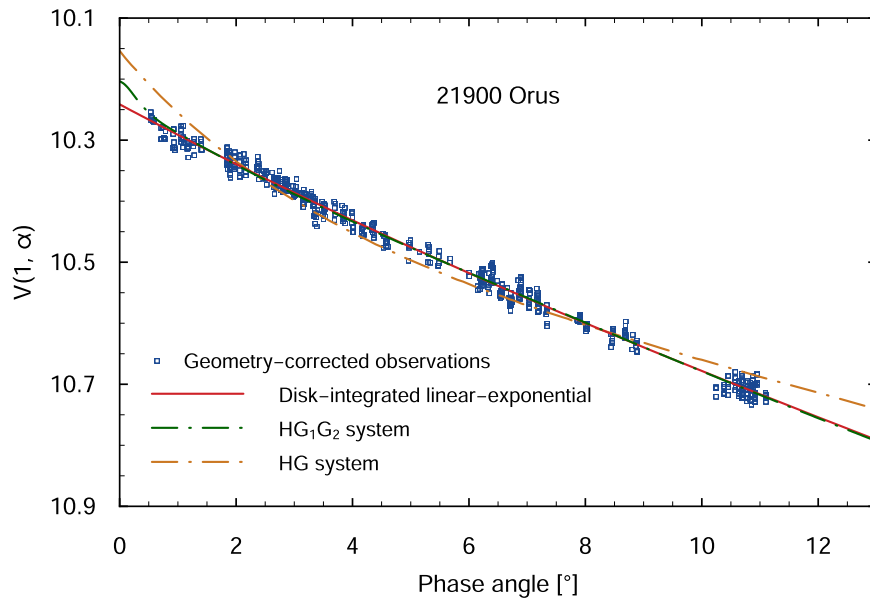
With an accuracy of the sidereal rotation period determination of about 10 and 61 ms for Eurybates and Orus, respectively, the rotation phase of these objects during the respective encounters with Lucy can be predicted with an uncertainty of a mere few degrees—precious information for the planning of the Lucy encounters.

During Lucy’s fly-by with Eurybates on 2027 August 12, the subsolar latitude will be  $-5^\circ$ . This geometry will allow Lucy to map the object up to very high latitudes, with a coverage of about 98% of the surface with a sampling better than  $500 \text{ m pixel}^{-1}$  and 60% better than  $100 \text{ m pixel}^{-1}$ . Orus’s subsolar latitude at the time of the Lucy close encounter on 2028 November 11 will be  $+22^\circ$ . This encounter geometry should enable Orus to be mapped for more than 90% of its entire surface with a spatial sampling better than  $1 \text{ km pixel}^{-1}$  and for more than 50% with a sampling better than  $100 \text{ m pixel}^{-1}$ .

Research at the DLR was funded by the DLR Programmatik Raumfahrtforschung und -technologie through the grant 2474029 Lucy. Part of this work was supported by the Lucy mission, which is funded through the NASA Discovery program on contract No. NNM16AA08C. This work was partly based on observations collected at the Centro Astronómico Hispano en Andalucía (CAHA) at Calar Alto. The DLR group would like to thank the Institute for Astrophysics of the University of Göttingen for granting time at the MONET South telescope to this project. The authors are indebted to Brian Keeney and coauthors for providing preliminary data from their occultation campaigns. The authors would also like to thank the two anonymous reviewers who, with their insightful comments, contributed to improving this paper. This research has made use of the NASA/IPAC Infrared Science Archive, which is funded by the National Aeronautics and Space Administration and operated by the California Institute of Technology. This work includes data from the Asteroid Terrestrial-impact Last Alert System (ATLAS) project. ATLAS is primarily funded to search for near-Earth asteroids through NASA grants NN12AR55G, 80NSSC18K0284, and



**Figure 15.** Occulting silhouettes of the best-fit convex model of Orus (solid black line) along with the rejected complementary model (displayed in light gray) at the time of the 2021 October 16 occultation. The blue line represents a negative detection. The red, green, and blue arrows represent the X-, Y-, and Z-axes in the body-fixed reference frame, respectively.



**Figure 16.** Sphere-integrated phase curve for Orus. The blue squares represent the geometry-corrected individual data points for the subset of the observations for which a reliable transformation to the Johnson  $V$  band could be determined.

80NSSC18K1575; by-products of the NEO search include images and catalogs from the survey area. The ATLAS science products have been made possible through the contributions of

the University of Hawaii Institute for Astronomy, the Queen's University Belfast, the Space Telescope Science Institute, and the South African Astronomical Observatory.

## Appendix

### $H, G_1, G_2$ Surface Phase Function for the Lommel–Seeliger–Lambert Disk Function

For the purpose of convex inversion we describe the photometric properties of the surface with a photometric function that is the product of a Lommel–Seeliger–Lambert disk function and a surface phase function (Kaasalainen et al. 2001; Schröder et al. 2013). The corresponding *radiance factor* ( $I/F$ ) can be written as

$$I/F = A_{\text{LSL}} \mu_0 \left( \frac{1}{\mu + \mu_0} + c \right) f(\alpha). \quad (\text{A1})$$

$A_{\text{LSL}}$  is the Lommel–Seeliger–Lambert albedo;  $\alpha$  is the solar phase angle;  $\mu_0$  and  $\mu$  are the cosines of the incidence and

$$f_{H,G_1,G_2}(\alpha) = \left( \frac{4}{3}c + 1 \right) \times \frac{G_1 \Phi_1(\alpha) + G_2 \Phi_2(\alpha) + (1 - G_1 - G_2) \Phi_3(\alpha)}{[4c/(3\pi) (\sin(\alpha) + (\pi - \alpha) \cos(\alpha)) + (1 + \sin(\alpha/2) \ln(\tan(\alpha/4)) \tan(\alpha/2))]} \quad (\text{A5})$$

emission angles, respectively; and  $c$  is the partition coefficient for the Lambert contribution. The term  $f(\alpha)$  is the surface phase function (expressed in intensity). One of the advantages of this formalism is that the disk and phase functions depend separately on the phase angle and on the incidence and emission angles. Furthermore, there exists an analytical expression for the integral of the Lommel–Seeliger–Lambert disk function over a sphere that allows direct computation of the disk-integrated phase function (see, e.g., Li et al. 2015, 2020; Mottola et al. 2020):

$$\Phi_{\text{LSL}}(\alpha) = \frac{[4c/(3\pi) (\sin(\alpha) + (\pi - \alpha) \cos(\alpha)) + (1 + \sin(\alpha/2) \ln(\tan(\alpha/4)) \tan(\alpha/2))]}{(4c/3 + 1)} \frac{f(\alpha)}{f(0)}, \quad (\text{A2})$$

with  $\alpha$  expressed in radians. A popular choice for the surface phase function is a simple three-parameter linear exponential function (Kaasalainen et al. 2001), which has proven to be quite successful for the purpose of shape inversion and has the form

$$f_{\text{lin-exp}}(\alpha) = A_0 e^{-\alpha/D} + k\alpha + 1. \quad (\text{A3})$$

Here  $A_0$  is the amplitude of the opposition surge,  $D$  is the angular width of the opposition region, and  $k$  is the slope of the linear part of the function. The function is normalized such that its linear component is unity at zero phase.

Alternatively to the linear exponential function, we propose the  $H, G_1, G_2$  surface phase function in conjunction with the Lommel–Seeliger–Lambert disk function, which has the property of producing an  $H, G_1, G_2$  disk-integrated phase function when the corresponding radiance factor is integrated over a sphere.

The  $H, G_1, G_2$  disk-integrated phase function (Muinonen et al. 2010), adopted by the IAU in 2010 and intended to

supersede the old HG system, is defined as

$$\Phi_{H,G_1,G_2}(\alpha) = G_1 \Phi_1(\alpha) + G_2 \Phi_2(\alpha) + (1 - G_1 - G_2) \Phi_3(\alpha), \quad (\text{A4})$$

where the  $\Phi_i(\alpha)$  functions (normalized to unity at zero phase) are defined in Muinonen et al. (2010) as cubic splines and in Penttilä et al. (2016) in tabulated form.

Analogously to Muinonen et al. (2015), we then define a two-parameter  $H, G_1, G_2$  surface phase function for the Lommel–Seeliger–Lambert disk function—also normalized to unity at zero phase—as




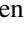
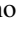


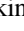
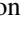
With this choice, the disk-integrated phase function for a sphere has the form of Equation (A4). By using Equation (A5) in conjunction with Equation (A1) during the optimization process, we can determine the  $G_1$  and  $G_2$  parameters directly during the inversion, simultaneously with the shape model and rotation state.

Given the used normalization, when using the  $H, G_1, G_2$  surface phase function for the Lommel–Seeliger–Lambert disk

function, the geometric albedo of a sphere is

$$p_V = A_{\text{LSL}} \left( \frac{1}{2} + \frac{2}{3}c \right). \quad (\text{A6})$$

## ORCID iDs

Stefano Mottola  <https://orcid.org/0000-0002-0457-3872>  
 Stephan Hellmich  <https://orcid.org/0000-0003-3997-3363>  
 Marc W. Buie  <https://orcid.org/0000-0003-0854-745X>  
 Robert D. Stephens  <https://orcid.org/0000-0002-0331-7404>  
 Mario Di Martino  <https://orcid.org/0000-0003-1265-1540>  
 Gerrit Proffe  <https://orcid.org/0000-0001-8678-9353>  
 Simone Marchi  <https://orcid.org/0000-0003-2548-3291>  
 Catherine B. Olkin  <https://orcid.org/0000-0002-5846-716X>  
 Harold F. Levison  <https://orcid.org/0000-0001-5847-8099>

## References

Bartczak, P., & Dudziński, G. 2018, *MNRAS*, 473, 5050  
 Bartczak, P., & Dudziński, G. 2019, *MNRAS*, 485, 2431

- Bellm, E. C., Kulkarni, S. R., Graham, M. J., et al. 2019, *PASP*, **131**, 018002
- Belskaya, I. N., & Shevchenko, V. G. 2000, *Icar*, **147**, 94
- Borucki, W. J., Koch, D., Basri, G., et al. 2010, *Sci*, **327**, 977
- Bowell, E., Hapke, B., Domingue, D., et al. 1989, in *Asteroids II*, ed. R. P. Binzel, T. Gehrels, & M. S. Matthews (Tucson, AZ: Univ. Arizona Press), 524
- Brož, M., & Rožehnal, J. 2011, *MNRAS*, **414**, 565
- Buie, M. W., Keeney, B., Levison, H., et al. 2020, AAS/DPS Meeting, **52**, 401.02
- Buie, M. W., Keeney, B. A., Strauss, R. H., et al. 2021, *PSJ*, **2**, 202
- Buie, M. W., Zangari, A. M., Marchi, S., Levison, H. F., & Mottola, S. 2018, *AJ*, **155**, 245
- Caramia, M., & Dell’Olmo, P. 2008, *Multi-objective Management in Freight Logistics* (London: Springer)
- Ďurech, J., & Kaasalainen, M. 2003, *A&A*, **404**, 709
- Emery, J. P., Burr, D. M., & Cruikshank, D. P. 2010, *AJ*, **141**, 25
- Evans, D. W., Riello, M., De Angeli, F., et al. 2018, *A&A*, **616**, A4
- Flewelling, H. A., Magnier, E. A., Chambers, K. C., et al. 2020, *ApJS*, **251**, 7
- Fornasier, S., Dotto, E., Hainaut, O., et al. 2007, *Icar*, **190**, 622
- Gaia Collaboration, Spoto, F., Tanga, P., et al. 2018, *A&A*, **616**, A13
- Grav, T., Mainzer, A. K., Bauer, J. M., Masiero, J. R., & Nugent, C. R. 2012, *ApJ*, **759**, 49
- Harris, A. W., & Harris, A. W. 1997, *Icar*, **126**, 450
- Harris, A. W., Young, J. W., Scaltriti, F., & Zappala, V. 1984, *Icar*, **57**, 251
- Helfenstein, P., & Veverka, J. 1989, in *Asteroids II*, ed. R. P. Binzel, T. Gehrels, & M. S. Matthews (Tucson, AZ: Univ. Arizona Press), 557
- Horn, B. K. P. 1984, *Proc. IEEE*, **72**, 1671
- IRSA 2022, Zwicky Transient Facility Image Service, IPAC, doi:10.26131/IRSA539
- Jaumann, R., Nathues, A., Mottola, S., & Hoffmann, H. 1996, Workshop on Evolution of Igneous Asteroids: Focus on Vesta and the HED Meteorites, Part 1 (Houston, TX: Lunar and Planetary Institute), 13
- Kaasalainen, M., & Ďurech, J. 2020, arXiv:2005.09947
- Kaasalainen, M., & Lamberg, L. 2006, *InvPr*, **22**, 749
- Kaasalainen, M., Lu, X., & Vanttinen, A.-V. 2012, *A&A*, **539**, A96
- Kaasalainen, M., Mottola, S., & Fulchignoni, M. 2002, in *Asteroids III*, ed. W. F. Bottke, Jr. et al. (Tucson, AZ: Univ. Arizona Press), 139
- Kaasalainen, M., & Torppa, J. 2001, *Icar*, **153**, 24
- Kaasalainen, M., Torppa, J., & Muinonen, K. 2001, *Icar*, **153**, 37
- Keeney, B., Buie, M., Kaire, M., et al. 2021, AGUFM, **2021**, P32B-03
- Lamberg, L. 1993, PhD thesis, Univ. Helsinki
- Lamberg, L., & Kaasalainen, M. 2001, *JCoAM*, **137**, 213
- Lebedev, V. I., & Laikov, D. N. 1999, *Doklady Mathematics*, **59**, 477
- Levison, H. F., Olkin, C., Noll, K. S., & Marchi, S. 2017, LPSC, **48**, 2025
- Levison, H. F., Olkin, C. B., Noll, K. S., et al. 2021, *PSJ*, **2**, 171
- Li, J. Y., Helfenstein, P., Buratti, B., Takir, D., & Clark, B. E. 2015, in *Asteroids IV*, ed. P. Michel, F. E. De Meo, & W. F. Bottke, Jr. (Tucson, AZ: Univ. Arizona Press), 129
- Li, J.-Y., Helfenstein, P., Buratti, B. J., Takir, D., & Clark, B. E. 2020, *Icar*, **337**, 113354
- Martikainen, J., Muinonen, K., Penttilä, A., Cellino, A., & Wang, X.-B. 2021, *A&A*, **649**, A98
- Milani, A., Knežević, Z., Spoto, F., et al. 2017, *Icar*, **288**, 240
- Minkowski, H. 1897, NWGot, 1897, 198, <https://eudml.org/doc/58391>
- Mottola, S., Di Martino, M., Erikson, A., et al. 2011, *AJ*, **141**, 170
- Mottola, S., Hellmich, S., Buie, M. W., et al. 2020, *PSJ*, **1**, 73
- Mottola, S., Marchi, S., Buie, M. W., et al. 2016, AAS/DPS Meeting, **48**, 208.04
- Muinonen, K., Belskaya, I. N., Cellino, A., et al. 2010, *Icar*, **209**, 542
- Muinonen, K., Wilkman, O., Cellino, A., Wang, X., & Wang, Y. 2015, *P&SS*, **118**, 227
- Noll, K. S., Brown, M. E., Weaver, H. A., et al. 2020, *PSJ*, **1**, 44
- Olkin, C. B., Levison, H. F., Vincent, M., et al. 2021, *PSJ*, **2**, 172
- Pál, A., Szakáts, R., Kiss, C., et al. 2020, *ApJS*, **247**, 26
- Penttilä, A., Shevchenko, V. G., Wilkman, O., & Muinonen, K. 2016, *P&SS*, **123**, 117
- Press, W. H., Teukolsky, S. A., Vetterling, W. T., & Flannery, B. P. 1992, *Numerical Recipes in FORTRAN: The Art of Scientific Computing* (2nd ed.; Cambridge: Cambridge Univ. Press)
- Ricker, G. R., Winn, J. N., Vanderspek, R., et al. 2014, *Proc. SPIE*, **9143**, 914320
- Roig, F., Ribeiro, A. O., & Gil-Hutton, R. 2008, *A&A*, **483**, 911
- Schröder, S. E., Mottola, S., Keller, H. U., Raymond, C. A., & Russell, C. T. 2013, *P&SS*, **85**, 198
- Shevchenko, V. G., Belskaya, I. N., Muinonen, K., et al. 2016, *P&SS*, **123**, 101
- Shevchenko, V. G., Belskaya, I. N., Slyusarev, I. G., et al. 2012, *Icar*, **217**, 202
- Souza-Feliciano, A. C., De Prá, M., Pinilla-Alonso, N., et al. 2020, *Icar*, **338**, 113463
- Stephens, R. D. 2010, MPBu, **37**, 47
- Stephens, R. D., & Warner, B. D. 2021, MPBu, **48**, 13
- Tedesco, E. F., Noah, P. V., Noah, M., & Price, S. D. 2004, IRAS Minor Planet Survey V6.0, NASA Planetary Data System, <https://pds.nasa.gov/ds-view/pds/viewProfile.jsp?dsid=IRAS-A-FPA-3-RDR-IMPS-V6.0>
- Tonry, J. L., Denneau, L., Heinze, A. N., et al. 2018, *PASP*, **130**, 064505
- Transtrum, M. K., Machta, B. B., & Sethna, J. P. 2011, *PhRvE*, **83**, 036701
- Transtrum, M. K., & Sethna, J. P. 2012, arXiv:1207.4999
- Usui, F., Kuroda, D., Müller, T. G., et al. 2011, *PASJ*, **63**, 1117
- Viikinkoski, M., Hanuš, J., Kaasalainen, M., Marchis, F., & Ďurech, J. 2017, *A&A*, **607**, A117
- Viikinkoski, M., Kaasalainen, M., & Ďurech, J. 2015, *A&A*, **576**, A8